Cell Reports

Article

MDC1 maintains active elongation complexes of RNA polymerase II

Graphical abstract

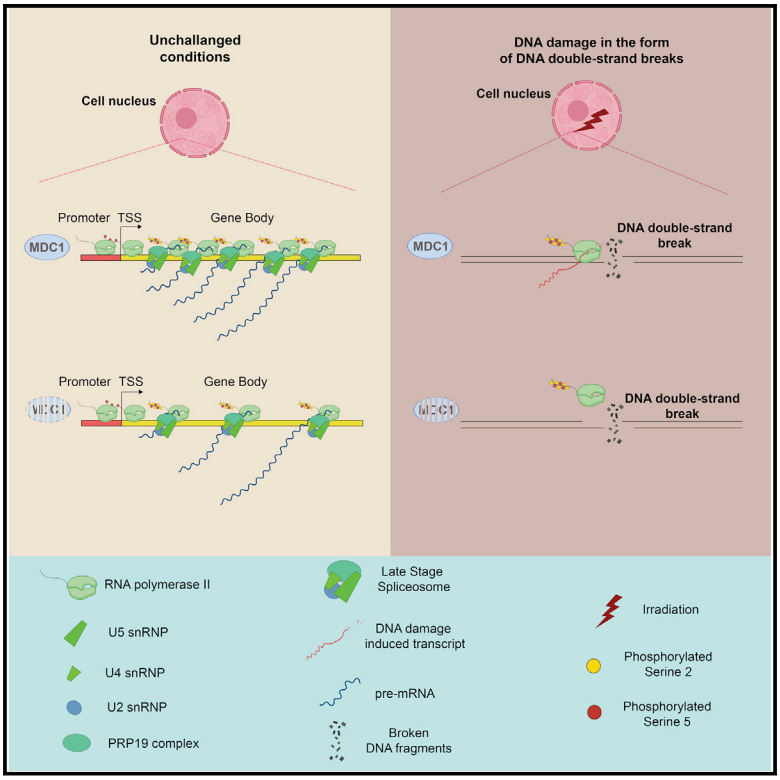

Highlights

- MDC1 regulates the abundance of the active RNAPII elongating complexes
- MDC1 affects spliceosome assembly, influencing pre-mRNA splicing
- MDC1 facilitates RNAPII-mediated nascent transcription at DNA double-strand breaks
- Low levels of MDC1 sensitize cancer cells to the CDK7 inhibitor THZ1

Authors

George Pappas, Sebastian Howen Nesgaard Munk, Kenji Watanabe, ..., Apolinar Maya-Mendoza, Panagiotis Galanos, Jiri Bartek

Correspondence

apomm@cancer.dk (A.M.-M.), panos@cancer.dk (P.G.), jb@cancer.dk (J.B.)

In brief

Pappas et al. show that MDC1 is necessary to regulate the RNA polymerase II (RNAPII)-dependent transcription in normal conditions and upon DNA damage. In MDC1-depleted cells, the abundance of the active RNAPII elongating complexes is decreased with a negative effect on splicing and repair.

Pappas et al., 2023, Cell Reports *42*, 111979
January 31, 2023
https://doi.org/10.1016/j.celrep.2022.111979

CellPress

Cell Reports

CellPress
OPEN ACCESS

Article

MDC1 maintains active elongation complexes of RNA polymerase II

George Pappas,[1,10] Sebastian Howen Nesgaard Munk,[2,10] Kenji Watanabe,[3] Quentin Thomas,[4,11] Zita Gál,[5,11] Helena Hagner Gram,[1,11] MyungHee Lee,[1,2] Daniel Gómez-Cabello,[6,7] Dimitris Christos Kanellis,[8] Pedro Olivares-Chauvet,[9] Dorthe Helena Larsen,[5] Lea Haarup Gregersen,[4] Apolinar Maya-Mendoza,[2,*] Panagiotis Galanos,[1,*] and Jiri Bartek[1,8,12,*]

[1]Genome Integrity Group, Danish Cancer Society Research Center, 2100 Copenhagen, Denmark
[2]DNA Replication and Cancer Group, Danish Cancer Society Research Center, 2100 Copenhagen, Denmark
[3]Cancer Institute, Japanese Foundation for Cancer Research, Tokyo 135-8550, Japan
[4]Department of Cellular and Molecular Medicine, University of Copenhagen (UCPH), 2200 Copenhagen, Denmark
[5]Nucleolar Stress and Disease Group, Danish Cancer Society Research Center, 2100 Copenhagen, Denmark
[6]Instituto de Biomedicina de Sevilla (IBiS), Hospital Universitario Virgen del Rocío/CSIC/Universidad de Sevilla, 41013 Seville, Spain
[7]Departamento de Genética, Facultad de Biología, Universidad de Sevilla, 41012 Seville, Spain
[8]Department of Medical Biochemistry and Biophysics, Division of Genome Biology, Karolinska Institutet, Science for Life Laboratory, 17177 Stockholm, Sweden
[9]Berlin Institute for Medical Systems Biology, Max Delbruck Center of Molecular Medicine, 13125 Berlin, Germany
[10]These authors contributed equally
[11]These authors contributed equally
[12]Lead contact
*Correspondence: apomm@cancer.dk (A.M.-M.), panos@cancer.dk (P.G.), jb@cancer.dk (J.B.)
https://doi.org/10.1016/j.celrep.2022.111979

SUMMARY

The role of MDC1 in the DNA damage response has been extensively studied; however, its impact on other cellular processes is not well understood. Here, we describe the role of MDC1 in transcription as a regulator of RNA polymerase II (RNAPII). Depletion of MDC1 causes a genome-wide reduction in the abundance of actively engaged RNAPII elongation complexes throughout the gene body of protein-encoding genes under unperturbed conditions. Decreased engaged RNAPII subsequently alters the assembly of the spliceosome complex on chromatin, leading to changes in pre-mRNA splicing. Mechanistically, the S/TQ domain of MDC1 modulates RNAPII-mediated transcription. Upon genotoxic stress, MDC1 promotes the abundance of engaged RNAPII complexes at DNA breaks, thereby stimulating nascent transcription at the damaged sites. Of clinical relevance, cancer cells lacking MDC1 display hypersensitivity to RNAPII inhibitors. Overall, we unveil a role of MDC1 in RNAPII-mediated transcription with potential implications for cancer treatment.

INTRODUCTION

Each cell in the human body is continuously subjected to environmental or endogenous insults that cause diverse DNA lesions, the most toxic of which are double-strand breaks (DSBs).[1] Upon DNA damage, cells trigger an intricate signaling network, termed DNA damage response (DDR), to deal with the lesions and maintain genomic integrity. One of the earliest events of the DDR is the recruitment of MDC1 (also known as NFBD1) ensuing the damage recognition. MDC1 acts as a scaffold protein that recruits and helps activate several downstream DDR factors, serving as the main signal transducer of the pathway.[2] Interestingly, early investigations indicated that MDC1 possesses a highly conserved transcription transactivation activity site within its amino acid residues 508–995.[3] However, MDC1's participation in transcription has remained understudied, being long overshadowed by its crucial role in the DDR.

Transcription is a tightly regulated process[4–8] that consists of three main steps in eukaryotes: initiation, elongation, and termination.[9–12] RNA polymerase II (RNAPII) is responsible for the transcription of protein-encoding genes as well as some non-coding RNAs. Moreover, the carboxy-terminal domain (CTD) of RNAPII is essential for the coordination of transcription and co-transcriptional processing, with the phosphorylation status of its serine residues (serine 2 and 5) being critical for the timely execution of each step.[13,14] Thus, dynamic RNAPII CTD phosphorylation mediates the coupling of pre-mRNA synthesis and pre-mRNA splicing, one of the main processing steps of nascent transcripts. Pre-mRNA splicing is the main determinant of the abundance and ratio of different transcript isoforms in the cells. Splicing is catalyzed by the spliceosome, a dynamic ribonucleoprotein complex composed of U1, U2, U5, and U4/U6 small nuclear ribonucleoprotein (snRNP) complexes as well as additional proteins (e.g., CDC5L, PLRG1) tightly linked to RNAPII elongation and CTD phosphorylation.[15,16] Therefore, fine-tuning of transcription and co-transcriptional processing is vital for the cells and important for genome integrity maintenance. Deregulation of these processes can lead to increased DNA damage and genomic instability.[17]

DNA damage is followed by repression of RNAPII-mediated transcription.[18] However, the ensuing activation of DDR has been recently shown to depend on the accumulation of nascent transcripts at the damaged sites besides the recruitment of DDR factors and chromatin configuration.[19,20] In fact, recent studies have unveiled a shift from the canonical to a non-canonical RNAPII-mediated transcription at the sites of DNA damage.[18,21–23] In the latter process, RNAPII becomes recruited to DSB sites and generates nascent long non-coding RNA transcripts which facilitate the recruitment of DDR proteins, promoting DSB signaling and repair.[24,25] Thus, evidence connecting DDR and transcription paves the way for the elucidation of a functional interplay between these two fundamental biological processes.

In the present study, we describe a role for MDC1 as a regulator of RNAPII, by maintaining the bound fraction of RNAPII elongation complexes on the DNA template. Depletion of MDC1 leads to a decrease in RNAPII-mediated transcription, independently of DDR and cell cycle progression. In parallel, low levels of MDC1 induce changes in cassette exons, thereby altering pre-mRNA splicing. Furthermore, we reveal an additional functional aspect of MDC1 in DDR as a mediator of DSB-induced nascent transcription. Consistent with our mechanistic findings, we report that a decrease in the abundance of MDC1 sensitizes human cancer cells to the CDK7 inhibitor THZ1, highlighting the clinical relevance of our findings.

RESULTS

MDC1 facilitates RNAPII activity

To investigate the role of MDC1 in transcription, we employed 5-bromouridine 5′-triphosphate (BrUTP) incorporation assay, a fluorescence-based method that measures the incorporation of 5-bromouridine 5′-triphosphate mediated by the chromatin-associated cellular transcription machinery.[26,27] In this assay, the permeabilization step and the short pulse of BrUTP treatment (8 min) allowed us to gain an immediate snapshot of the ongoing nascent transcription mediated by the chromatin-engaged fraction of RNA polymerases. Ablation of MDC1 with small interfering RNA (siRNA) (Figures S1A and S1B) reduced transcription in human U2OS cells (Figures 1A and 1B). The effect of MDC1 depletion on the transcription was evident even from the first 6 h following siRNA transfection (Figures S1C and S1D). The same results were obtained with two additional independent siRNAs (Figures S1E and S1F). By quantifying the BrUTP signal in the two main compartments of the nucleus (Figures S1G and S1H), we observed that the "nucleolar" transcription remained unaffected, while the "nuclear," excluding the nucleolar signal, was reduced upon MDC1 depletion (Figures 1C and 1D). RNAPII is the predominant enzyme that carries out the transcription of the nuclear DNA outside the nucleoli.[28] Cells exposed to THZ1 or 5,6-dichloro-1-beta-D-ribofuranosylbenzimidazole (DRB), which respectively inhibit CDK7 and CDK9 kinase, known to regulate the RNAPII transcription cycle, displayed a significant decrease in the incorporation of the BrUTP (Figures S1I and S1J).[29,30] Treating cells with 5′-ethynyl uridine (EU) as an alternative means of measuring transcription rates showed a similar decrease in MDC1-depleted cells (Figures S2A and S2B). Moreover, reconstitution of MDC1 using a siRNA-resistant plasmid in cells with depleted endogenous protein restored the transcriptional activity (Figure 1E). These results were cell type-independent, as transcription was similarly decreased in other cancer and near normal cell lines upon depletion of MDC1 (Figure 1F). Altogether, these findings suggest that MDC1 facilitates RNAPII-mediated transcription.

To gain more mechanistic insights into this function of MDC1, we complemented MDC1-depleted U2OS cells with ectopic siRNA-resistant wild-type (WT) or mutant MDC1 plasmids lacking different functional domains and then monitored transcription activity by EU incorporation coupled with quantitative image-based cytometry (QIBC)[31] (Figures S2C–S2E). While introducing WT MDC1 restored the ongoing transcription confirming our previous results, we detected repressed transcriptional activity upon ectopic expression of MDC1 lacking S/TQ (Figure S2D). This finding indicated S/TQ, a well-characterized domain implicated in the DDR,[32–35] as the responsible functional domain of MDC1 involved in promoting RNAPII-mediated transcription.

MDC1 has been identified as an adaptor protein facilitating cell cycle progression.[36–39] We, therefore, asked whether the observed transcriptional suppression in the absence of MDC1 might reflect alterations in the cell cycle, causing in turn defects in transcription. From profiling the cell cycle of U2OS cells depleted of MDC1, we did not observe any significant changes in cell cycle progression (Figures S2F and S2G). Moreover, we investigated whether MDC1 depletion itself could indirectly suppress transcription by inducing DNA damage.[18] To address that, we measured γH2AX and 53BP1 foci formation as surrogate markers of DNA damage and repair. MDC1 depletion did not enhance DNA damage on the basis of the γH2AX foci formation, while the 53BP1 foci number was reduced, supporting the upstream role of MDC1 in the recruitment of 53BP1 to damage sites (Figure S2H).[40,41] Next, we asked whether the observed MDC1-dependent transcriptional phenotype could be mediated by 53BP1 as the downstream effector. Notably, such an MDC1-53BP1 axis was not found to be responsible for the observed alterations in RNAPII-mediated transcription indicating a role independent of 53BP1 (Figure S2I). Altogether, our results pointed to an important role of MDC1 in transcription as a regulator of RNAPII activity in a cell cycle- and DDR-independent manner.

MDC1 depletion impairs the elongation phase of RNAPII-mediated transcription

To elucidate how MDC1 regulates transcription, we first analyzed interactions of MDC1 with RNAPII. Indeed, MDC1 interacts with RNAPII via protein-protein interactions, as part of the RNAPII transcription complex (Figure 2A). Proper dynamic phosphorylation of the RNAPII CTD is a prerequisite for the RNAPII-mediated transcriptional process.[13] Therefore, we analyzed the chromatin-bound fraction of RNAPII and the phosphorylation of serine 5 (pSer5) and serine 2 (pSer2) of RNAPII CTD tail, as markers of the initiation and elongation RNAPII complexes, respectively, using phospho-specific antibodies (Figure S2J).[42,43] By using QIBC, we observed neither alteration of the total RNAPII chromatin-bound fraction nor of the Ser5 phosphorylation upon MDC1 knockdown (Figures 2B and 2C). However, the level of the elongation phospho-mark, pSer2, was found to be reduced (Figure 2D). Alterations in pSer2 of CTD

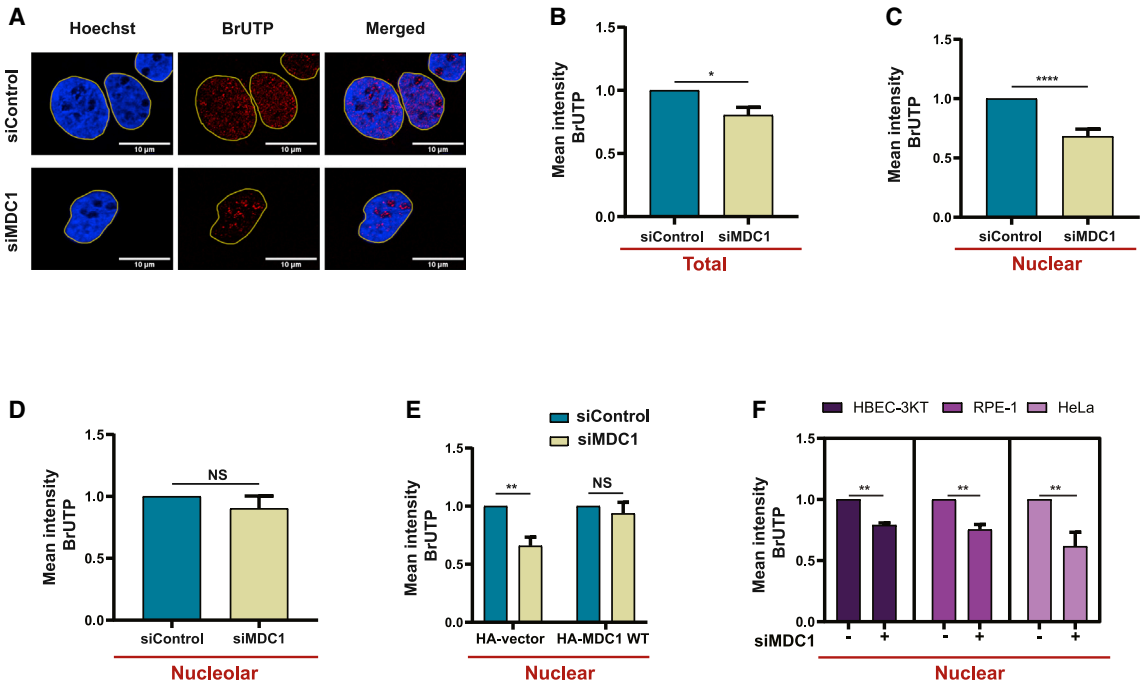

Figure 1. MDC1 facilitates RNAPII activity

(A) Representative images of U2OS nascent RNA synthesis on the basis of BrUTP incorporation, upon transfection with the indicated siRNAs. Scale bar represents 10 µm.

(B) Relative quantification of nascent RNA synthesis in the whole nucleus of U2OS cells ("nucleolar" and "nuclear" signal with subtracted nucleoli, indicated as total) transfected with the indicated siRNAs (number of biological replicates: n = 3). Biological replicates have been pooled together, and data are represented as mean ± standard error of the mean (SEM).

(C) Relative quantification of nuclear nascent RNA synthesis in U2OS cells transfected with the indicated siRNAs (number of biological replicates: n = 5). Biological replicates have been pooled together, and data are represented as mean ± SEM.

(D) Relative quantification of nucleolar nascent RNA synthesis in U2OS cells transfected with the indicated siRNAs (number of biological replicates: n = 4). Biological replicates have been pooled together, and data are represented as mean ± SEM.

(E) Relative quantification of nuclear nascent RNA synthesis in U2OS cells transfected with the indicated siRNAs (number of biological replicates: n = 3). Biological replicates have been pooled together, and data are represented as mean ± SEM.

(F) Relative quantification of nuclear nascent RNA synthesis in HeLa, HBEC-3KT and RPE-1 cells transfected with the indicated siRNAs (number of biological replicates: n = 3). Biological replicates have been pooled together, and data are represented as mean ± SEM.

NS, not significant; *p < 0.05; **p < 0.01; ****p < 0.0001, by unpaired Student's t test.

suggest aberrant RNAPII transcription in the productive elongation phase of the transcription cycle.[11,13] To test such possibility, we performed the DRB-release-quantitative real-time PCR assay.[44] Upon DRB addition, RNAPII stalls at promoter-proximal regions and upon drug removal, elongation can proceed in a synchronous manner.[45,46] We detected the levels of pre-mRNA for a selected gene, *ITPR1*, that served as an endogenous reporter and marker of transcription dynamics, via quantitative real-time PCR. Then, we quantified *ITPR1* pre-mRNA synthesis by using primers spanning intron-exon junctions at several time points following release from DRB (Figure 2E).[45] Upon MDC1 knockdown, the amplified product of the exon 1-intron 1 (Ex1/In1) region that lies proximal to the transcription start site (TSS) displayed no difference compared with the control conditions, suggesting that the initiation-to-elongation transition of RNAPII remained unaltered (Figure 2F). In contrast, the detection of exon 5-intron 5 (Ex5/In5) product was delayed by 15 min in cells with MDC1 knockdown, indicating either a slower transcription elongation rate or lower abundance of RNAPII elongation complexes along the gene body of *ITPR1* gene (Figure 2G). Moreover, we performed recovery experiments upon DRB treatment to confirm the observed phosphorylation patterns of RNAPII CTD upon MDC1 knockdown. DRB removal restored the levels of the initiation marker pSer5 with similar efficiency between control and MDC1-depleted cells, while the elongating marker pSer2 showed delayed recovery, corroborating the hypothesis of an impaired productive elongation phase in MDC1-depleted cells (Figures 2H and 2I). Consistently, we also observed lower BrUTP incorporation at each time point following DRB release upon MDC1 knockdown (Figure 2J). Together these observations suggest that MDC1 regulates RNAPII-mediated transcription by promoting the elongation phase.

MDC1 affects the engagement of RNAPII elongation complexes on the transcribing DNA template

Our results so far indicated impairment in the elongation process of transcription upon MDC1 knockdown, however, it was unclear whether this phenotype reflected a reduction of the

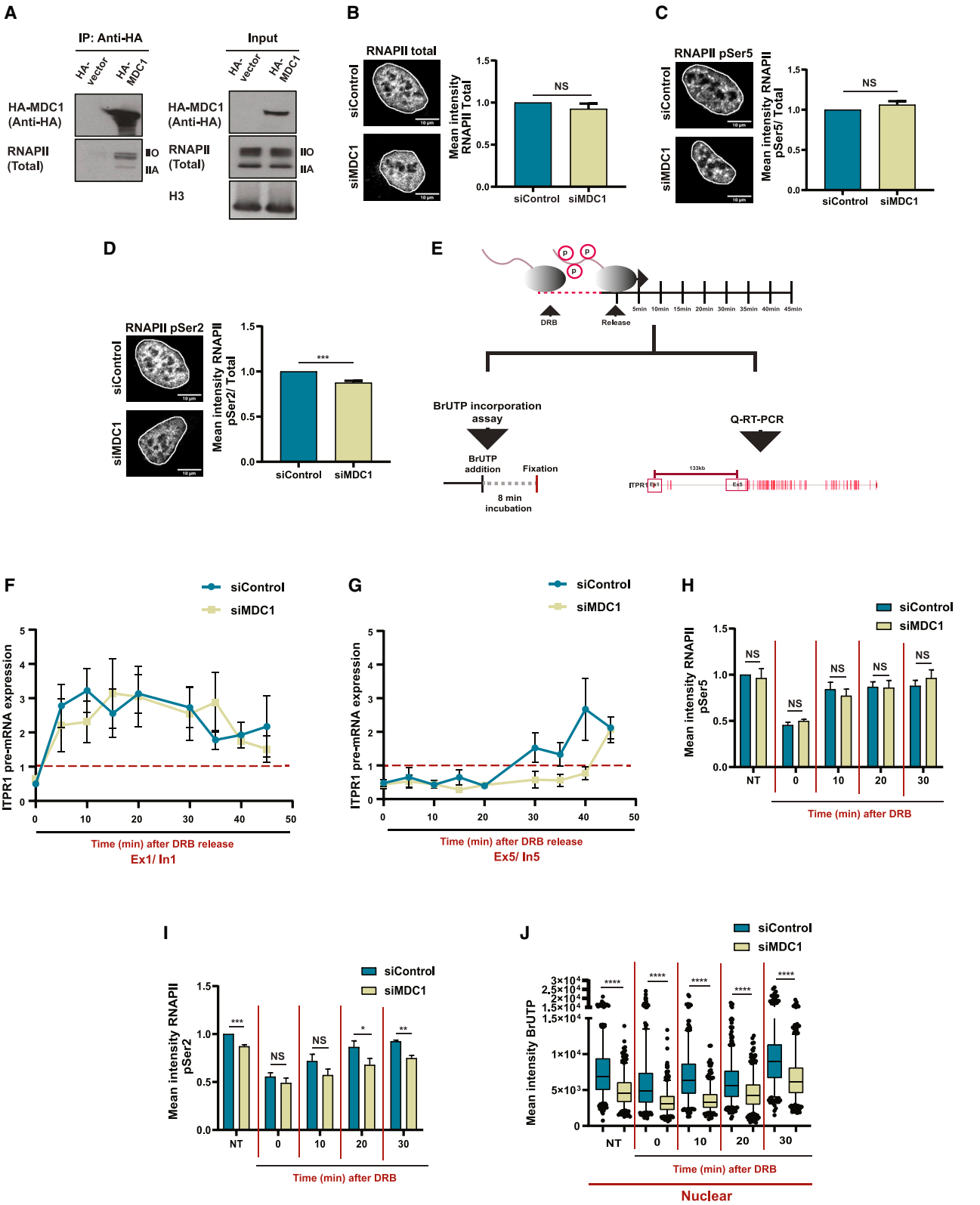

(legend on next page)

transcriptional speed or the number of actively engaged RNAPII. To answer this, we employed a recently established genome-wide approach, DRB/TT$_{chem}$-seq, to profile the ongoing nascent transcription.[47] With this approach, the transcription cycles of the cells were synchronized by DRB treatment, as previously described.[47] Cells were then released from the inhibitory effect of DRB, and transcription kinetics were monitored on the basis of the incorporation of 4-thiouridine (4sU) at distinct time points after release (Figures 3A and S3A). Importantly, yeast spike-ins of 4sU-labeled RNA served as a normalization control allowing the quantification of changes in overall levels of nascent transcription (Figure S3A). By using two biological replicates for each time point after DRB release (10, 20, 30 and 40 min), we observed a clear reduction of nascent transcription levels following DRB release at all 4-time points for MDC1-depleted cells compared with their mock-treated counterparts (Figures 3B and S3B). This effect was independent of gene length (Figures S3C and S3D). However, when tracking the RNAPII wave front, the engaged RNAPII complexes progressed through the gene body at rates similar to those of control cells (Figures 3B–3D and S3E). Thus, our findings demonstrate that MDC1 depletion does not affect the RNAPII elongation rate, but rather affects the abundance of the actively engaged RNAPII complexes on the DNA template in a global whole-genome scale (Figure 3E).

MDC1 knockdown induces changes in pre-mRNA splicing

Alterations in transcription dynamics and post-translational modifications in RNAPII CTD have been shown to influence pre-mRNA processing.[48–50] Pre-mRNA splicing is a central step of pre-mRNA processing, coupled to transcription.[48,51] Notably, we found that MDC1 binds to several components of the core spliceosome via protein-protein interactions, including snRNP proteins of both U2 (SF3B2) and U5 (PRP8) complexes as well as proteins of the core PRP19 complex (CDC5L and PLRG1) (Figures 4A and 4B), which is part of the late-stage spliceosome.[52] Additionally, depletion of MDC1 led to decreased protein-protein interactions among splicing factors (Figures 4C and S4A). Interestingly, we also observed a reduction of splicing factors abundance on chromatin, indicating altered kinetics in spliceosome assembly (Figures 4D and S4B). As a positive control, cells were treated with UVC (30 J/m^2) (Figures S4B).[53] Pre-mRNA splicing is carried out in a co-transcriptional manner taking place right after pre-mRNA synthesis. By performing the DRB-release-quantitative real-time PCR assay, we measured the rate of the splicing process that occurs in a co-transcriptional fashion on the basis of specific primers targeting *OPA1* pre-mRNA,[45] serving as an endogenous reporter (Figure 5A). MDC1-depleted cells displayed similar pre-mRNA splicing rates to their control counterparts as determined by the time between the detection of the newly synthesized exon (exon 19-intron 19) and the appearance of the splicing product of that exon and the immediately preceding exon (exon 18-intron 19) (Figures 5B and 5C). Collectively, these results suggest that a lower abundance of MDC1 leads to a decrease in spliceosome assembly, possibly because of reduced engaged RNAPII complexes, although without affecting splicing rates.

Impediments in pre-mRNA spliceosome assembly could potentially lead to genome-wide alternative splicing events, affecting isoform abundance and subsequently cellular homeostasis.[54] To test this hypothesis, we performed nanopore sequencing to use the exon connectivity information captured by long reads for alternative splicing analysis. In addition to the knockdown of MDC1, cells depleted for PLRG1 (Figure S5A) or treated with a low concentration of the splicing inhibitor pladienolide B (PLAB) were included in our experimental setup as known splicing-deficient conditions.[52,55] Similar to MDC1 depletion, PLRG1 depletion and PLAB treatment impaired nascent transcription (Figure S5B), further indicating the interconnection between transcription and splicing. The long-read workflow FLAIR (Full-Length Alternative Isoform analysis of RNA) was used to analyze splicing changes.[56] Analysis of alternative splicing events revealed that MDC1 depletion induced splicing alterations but to a lower extent compared with PLRG1 depletion (Figures 5D and 5E). Depletion of either MDC1 or PLRG1 resulted in changes in cassette exons, while intron retention was the predominant splicing alteration induced by PLAB (Figure 5E). Principal component analysis of isoform expression showed a separation between the known splicing-deficient conditions (siPLRG1 and PLAB) and the control, and a less distinct separation between the control and MDC1-depleted cells (Figure 5F). Global effects on transcript levels were not detectable because of sequencing library and data normalization. Consistently, we also found changes in isoform usage following MDC1 depletion or upon treatment with PLAB and to a greater extent in PLRG1-depleted cells (Figure 5G). We chose two significantly altered cassette exons induced by MDC1 depletion which were

Figure 2. MDC1 affects the transcription elongation phase

(A) Protein-protein interactions between HA-MDC1_WT and RNAPII (IIO, phosphorylated RNAPII; IIA, non-phosphorylated RNAPII).

(B) Relative quantification of total RNAPII chromatin-engaged fraction in U2OS cells transfected with the indicated siRNAs (number of biological replicates: n = 4). Biological replicates have been pooled together, and data are represented as mean ± SEM. Scale bars represent 10 μm.

(C and D) Relative quantification of RNAPII pSer2 and pSer5 chromatin-engaged fraction in U2OS cells transfected with the indicated siRNAs (number of biological replicates: n = 4 and n = 3 for pSer5 and pSer2, respectively). Biological replicates have been pooled together, and data are represented as mean ± SEM. Scale bars represent 10 μm.

(E) Schematic representation of DRB release-qPCR and DRB release-BrUTP incorporation assay.

(F and G) Nascent pre-mRNA synthesis of different regions of *ITPR1* gene in U2OS cells treated with the indicated siRNAs (number of biological replicates: n = 3). Biological replicates have been pooled together, and data are represented as mean ± SEM.

(H and I) Quantification of RNAPII pSer2 and pSer5 chromatin-engaged fraction in U2OS cells transfected with the indicated siRNAs following DRB release (number of biological replicates: n = 3). Biological replicates have been pooled together, and data are represented as mean ± SEM.

(J) Quantification of nuclear nascent RNA synthesis in U2OS cells transfected with the indicated siRNAs following DRB release (number of cells: n > 150). Values have been pooled together, and data are represented as mean ± SEM.

NS, not significant; *p < 0.05; **p < 0.01; ***p < 0.001; ****p < 0.0001, by unpaired Student's t test.

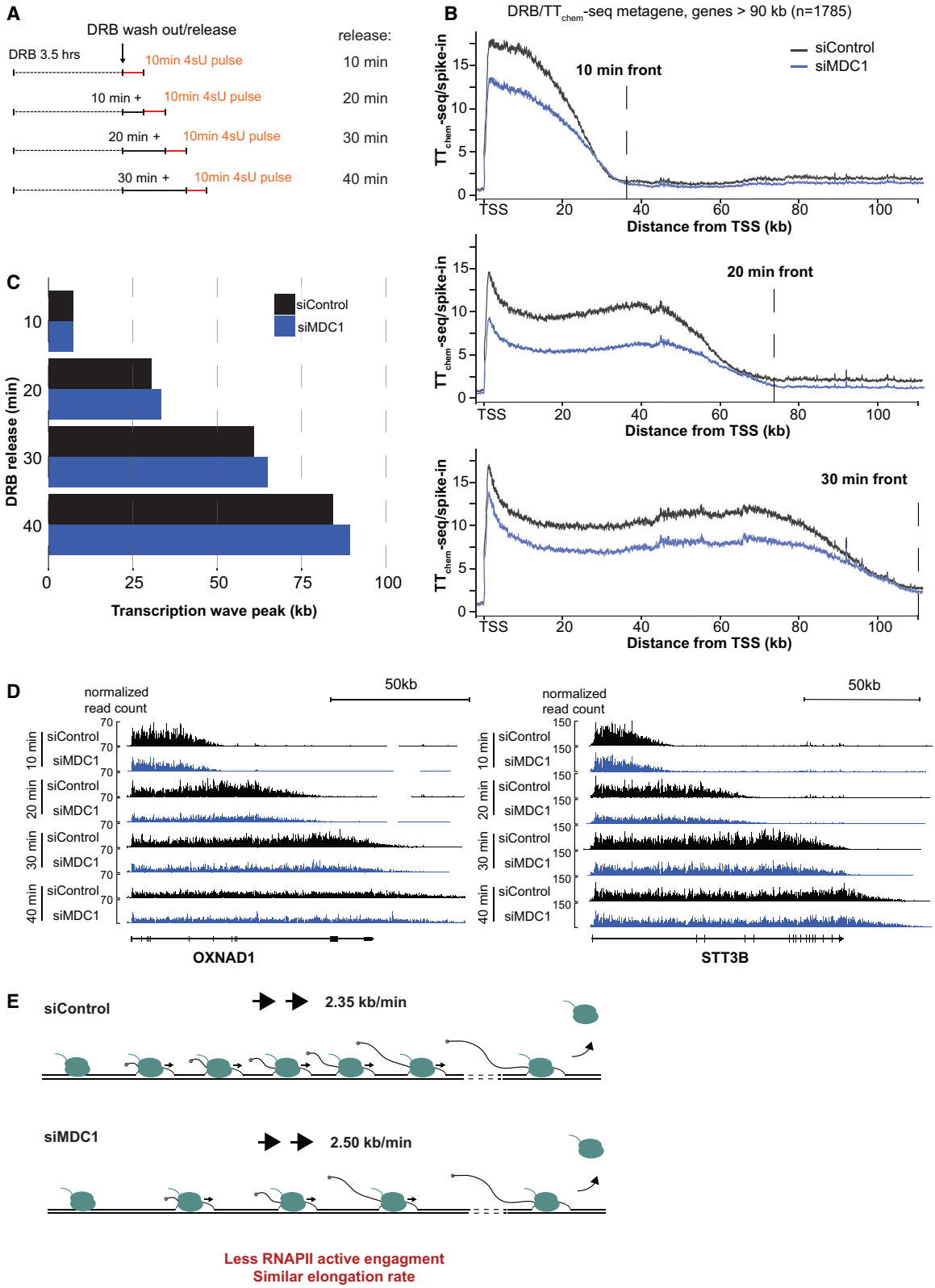

(legend on next page)

validated by quantitative real-time PCR (Figures S5C–S5H). Altogether, these observations indicated a subtle impact of MDC1 on pre-mRNA splicing occurring either in parallel or as a secondary effect caused by the global alterations of RNAPII processivity.

MDC1 is required for RNAPII-mediated nascent transcription at DSBs

RNAPII-mediated transcription is suppressed upon DNA damage; however, a non-canonical local transcription is triggered on damaged sites by the same enzyme promoting DDR activation and facilitating DNA repair.[20,57] Given the central function of MDC1 in DDR and the emerging role in transcription identified in our presented study, we hypothesized that there is a potential link between the role of MDC1 in transcription and DDR. While protein-protein interactions between MDC1 and RNAPII remained unaltered upon ionizing radiation (Figure S6A), suppression of transcription upon MDC1 depletion was even more pronounced following X-ray- or laser microirradiation (UVA)-inflicted DSBs (Figures 6A and S6B). To investigate whether MDC1 also plays a role in the non-canonical wave of transcription triggered at DSBs, we first monitored the abundance of EYFP-tagged α-amanitin-resistant RPB1 subunit of RNAPII (pYFP-RPB1aAmr) on damaged sites following laser microirradiation-induced DSBs (Figures 6B–6D). Upon treatment with α-amanitin, endogenous RNAPII was degraded and the abundance of pYFP-RPB1aAmr was measured at the damaged sites (Figures 6C and 6D). Notably, pYFP-RPB1aAmr displayed reduced engagement at the damaged sites upon MDC1 knockdown (Videos S1 and S2). Recent evidence supports the establishment of functional transcription promoters at DSB sites where γH2AX colocalizes with RNAPII and proteins of the pre-initiation complex (PIC).[58] In line with these data, we found that RNAPII interacts with γH2AX via protein-protein interactions following ionizing radiation (Figures S6C and S6D). Interestingly, MDC1 depletion led to decreased protein-protein interactions between RNAPII and γH2AX at such X-ray-induced DSBs (Figures S6C and S6D). However, we did not observe any significant alterations regarding MDC1 early recruitment kinetics on damaged chromatin in U2OS cells upon DRB treatment (Figure 6E; Videos S3 and S4), highlighting MDC1's upstream role in regulating the engagement of RNAPII at DNA damaged sites.

Next, we investigated MDC1's involvement in the *de novo* synthesis of transcripts at DSBs. Transcription at DSBs is one of the earliest steps in DDR.[58] Here, we combined BrUTP incorporation with laser microirradiation, allowing us to acquire direct snapshots of nascent ongoing transcription at the damaged sites (Figures 7A and 7B). Nascent transcription was significantly increased in the first 5 min following DSBs formation, while treatment with DRB was used as our negative control leading to reduced BrUTP signal at damaged sites in a time-dependent manner (Figure S6E). Importantly, depletion of MDC1 reduced BrUTP incorporation at the damaged sites (Figures 7C and 7D). Collectively, these findings indicate an upstream role of MDC1 as a DDR and transcription adaptor in the regulation of *de novo* RNAPII-mediated RNA synthesis on DSB sites.

MDC1 depletion sensitizes cancer cells to RNAPII inhibitors

Cancer cells display increased sensitivity to THZ1, a well-characterized CDK7 inhibitor that impairs RNAPII-mediated transcription.[59] Therefore, we asked whether MDC1 could affect the cellular response to such pharmacological inhibition of transcription. U2OS osteosarcoma cells were treated with different doses of THZ1, and the percentage of dead cells was quantified. In MDC1-knockdown cells, the fraction of dead cells almost doubled after treatment with THZ1 in a dose-dependent manner, compared with the effect of THZ1 in MDC1-proficient U2OS control cells (Figure 7E). Additionally, RPE-1 near normal human epithelial cells showed similar sensitivity to THZ1 upon MDC1 depletion, however to a lesser extent compared with U2OS cells (Figure S7A). To exclude that cell death was caused by accumulated DNA damage upon THZ1 treatment in MDC1-depleted cells, we monitored γH2AX foci formation with QIBC. Indeed, there was no increased DNA damage observed in either condition upon increasing doses of THZ1 (Figures S7B–S7E). Moreover, CDK7 is a well-characterized CDK-activating kinase (CAK) affecting cell cycle progression,[29] however no cell cycle alterations were observed upon THZ1 treatments in our experimental setup (Figures S7D and S7E). These results highlight the relevance of the levels of MDC1 to predict the sensitivity of cancer cells to transcription inhibitors.

DISCUSSION

The functional interplay between DNA damage and transcription has been in the spotlight of research in recent years.[18,20,21,24,57,58,60,61] These studies elucidated the activation of transcription to facilitate the repair process at the sites of DNA damage in coordination with DDR factors. However, little is known about the mechanistic involvement of the DDR factors in the regulation of transcription under unchallenged conditions. In the present study, we provide evidence for the role of the DDR factor MDC1 in the transcriptional dynamics and pre-mRNA splicing.

Initially, MDC1 was identified as a nuclear binding factor (NFBD1) with a potential transcription transactivation activity.[3] Later, a few studies have reported MDC1's role either as a transcriptional co-regulator of estrogen receptor α (ERα) and

Figure 3. MDC1 affects the engagement of RNAPII elongation complexes

(A) Principle of DRB release assay. Early RNAPII elongation is inhibited by DRB for 3.5 h and washed with PBS, followed by medium replacement. Nascent RNA is then labeled *in vivo* by the addition of 4sU for 10 min directly to the tissue culture medium at time-dependent release after DRB treatment to monitor how RNAPII progresses throughout the gene body.

(B) Metagene profile representing the average coverage normalized over spike-in and anchored at the TSS of non-overlapping protein-encoding genes with size above 90 kb (n = 1,785). Wavefront shows the end of the transcription progression wave at 10, 20, and 30 min.

(C) Measure of RNAPII transcription wave peak for siControl (black) and siMDC1 (blue) samples on the basis of highest peak values from the metagene profile.

(D) BigWig coverage profiles of DRB/TT_{chem}-seq results for *OXNAD1* and *STT3B*. The siControl samples are in black and siMDC1 samples are in blue.

(E) Schematic model of RNAPII active engagement and elongation speed upon MDC1 gene silencing versus control conditions.

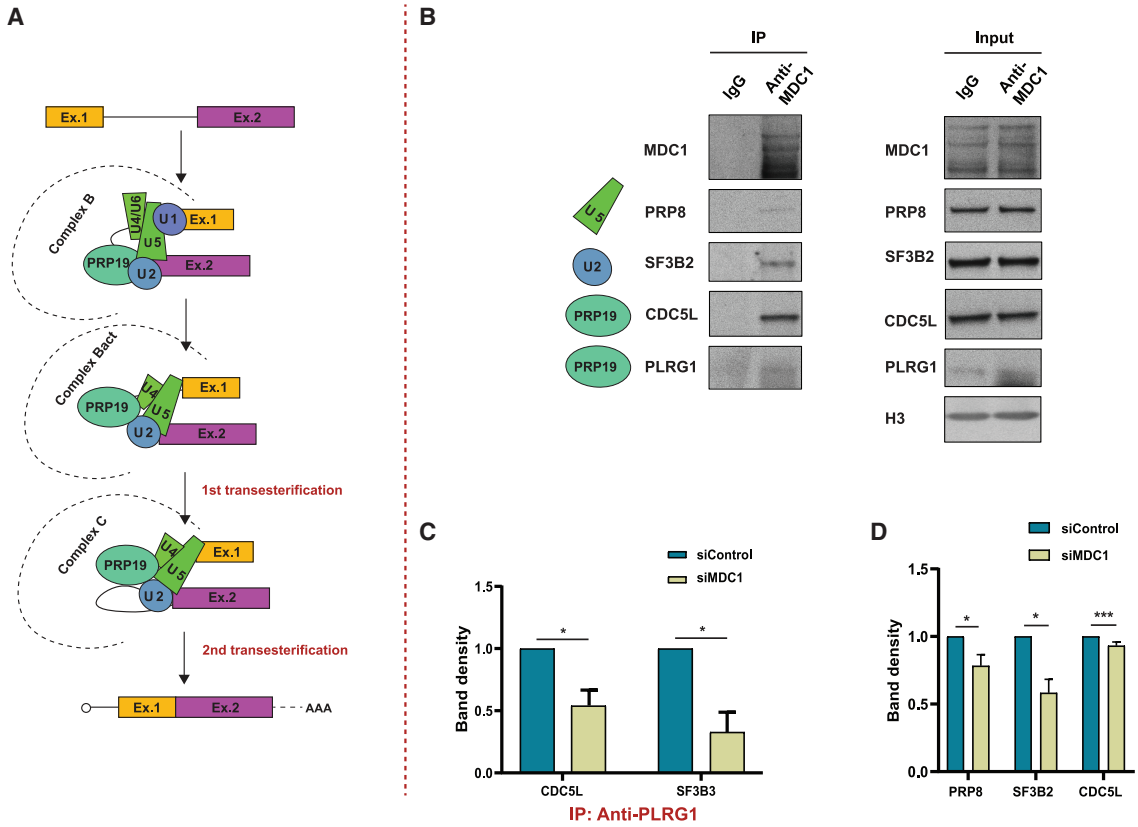

Figure 4. MDC1 knockdown affects spliceosome assembly

(A) Schematic representation of late-stage spliceosome snRNP (U2, U4, U5) and non-snRNP (PRP19) proteins.

(B) Protein-protein interactions between endogenous MDC1 and snRNP/non-snRNP proteins.

(C) Relative semi-quantification of protein-protein interactions between splicing factors upon transfection with the indicated siRNAs (number of biological replicates: n = 3). Biological replicates have been pooled together, and data are represented as mean ± SEM.

(D) Relative semi-quantification of chromatin-engaged fractions of splicing proteins in cells upon transfection with the indicated siRNAs (number of biological replicates: n = 3). Biological replicates have been pooled together, and data are represented as mean ± SEM.

*p < 0.05; ***p < 0.001, by unpaired Student's t test.

androgen receptor (AR) in breast and prostate cancer, respectively, or as a direct interactor with RNAPII, however without providing any direct mechanistic insights into the transcription process.[62–64] In the present study, we provide evidence that MDC1 plays an active role in RNAPII-mediated transcription. Specifically, we propose that MDC1 has a regulatory role in the productive elongation phase of the transcription cycle. Although the elongation rate was unaffected and RNAPII retained the same speed of transcription upon MDC1 depletion, we demonstrate a genome-wide role of MDC1 as a regulator of active RNAPII engagement (Figure 3E). Further corroborating our data, we also demonstrate that MDC1 interacts with components of the PRP19 complex (CDC5L and PLRG1; Figure 4B), which have been shown to regulate RNAPII-mediated transcription during the elongation process.[65]

Consistent with reduced RNAPII engagement within the gene body, depletion of MDC1 led to reduced phosphorylation of Ser2 residues of CTD. We show that the S/TQ domain of MDC1 is required for such role of MDC1 in facilitating transcription. The initial report on MDC1 (previously designated as *NFBD1* or *KIAA0170*) proposed the S/TQ region as crucial to activate transcription, whereas other candidate regions of the protein such as the tBRCT domain failed to show a similar impact on transcription,[3] supporting our data. It is well established that CTD phosphorylation and co-transcriptional splicing are coupled.[7,15] Here, we show that MDC1 regulates spliceosome assembly kinetics leading to subtle changes in pre-mRNA splicing and subsequently to altered isoform abundance. Our data define the role of MDC1 as a chromatin-binding adaptor protein that interacts both with RNAPII and with spliceosomal subunits, thereby coordinating RNAPII engagement and splicing efficiency.

Additionally, our findings reveal a functional aspect of MDC1 in DDR, as a facilitator of RNAPII-mediated DNA damage-induced *de novo* RNA synthesis at DSBs via regulating the amount of engaged RNAPII complexes on the damage sites. In the present study, we show that MDC1 interacts with RNAPII both in unchallenged conditions and upon DSB formation. Our data indicate that MDC1 is responsible for the engagement of RNAPII on the DNA template regulating both canonical and non-canonical routes of DNA transcription. By establishing an experimental

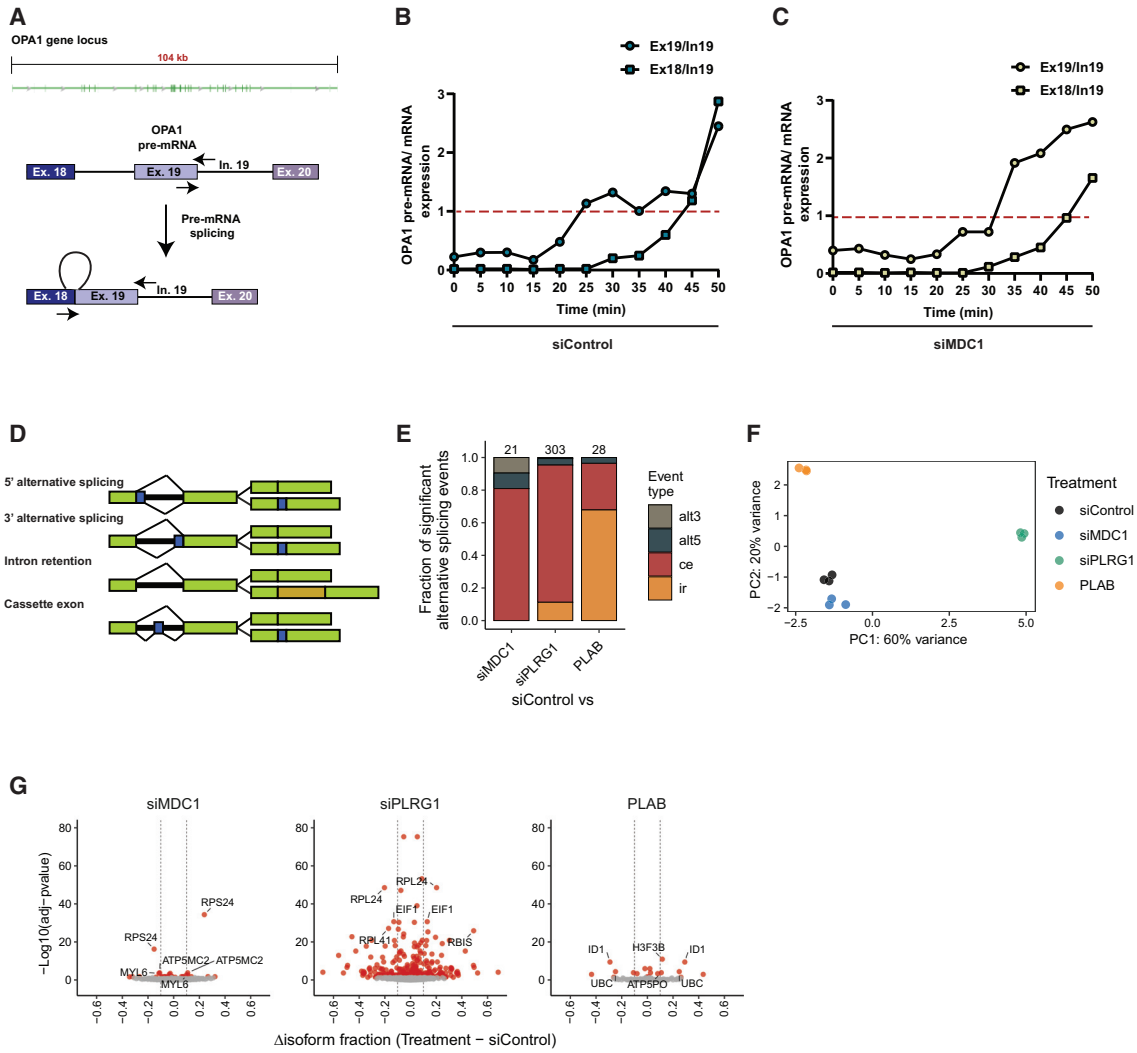

Figure 5. MDC1 induces changes in pre-mRNA splicing

(A) Schematic representation of the DRB release-qPCR assay used to monitor pre-mRNA splicing kinetics. Black arrows indicate the two sets of primers used for the amplification of exon 19-intron 19 (Ex19/In19) and exon 18-intron 19 (Ex18/In19) sequences of *OPA1* gene.

(B and C) Analysis of splicing kinetics of *OPA1* gene in U2OS cells transfected with the indicated siRNAs.

(D) Schematic representation of the alternative splicing events assayed in 5E.

(E) Distributions of significant alternative splicing events (adjusted $p < 0.05$) for the indicated comparisons. Event types: alt3, alternative 3′ splicing; alt5, alternative 5′ splicing; ce, cassette exon; ir, intron retention. The total number of significant events for each comparison is indicated above the bars.

(F) PCA of isoform expression in the samples (n = 3). PC1 and PC2 denote principal components 1 and 2, respectively.

(G) Volcano plots of differentially used isoforms after the indicated treatments. Isoforms with significant usage changes are in red (adjusted $p < 0.05$) while non-significant changes are in gray. In each plot, the top 6 significant isoforms with large usage changes (Δisoform fraction > 0.1) are indicated with gene names.

setup that combines UVA laser ablation and BrUTP incorporation assay, we provide robust evidence of a role of MDC1 as an upstream regulator of DSB-induced *de novo* RNAPII-mediated RNA synthesis, thereby uncovering a missing link in the interplay between DDR and transcription at the DSB sites. NBS1 protein has been recently shown to be indispensable for RNAPII activity at DSBs by mediating the melting of DNA strands, affecting local chromatin conformation.[25] Hence, the upstream role of MDC1 in NBS1 chromatin retention at DSB sites[41,66,67] could potentially suggest an as yet uncharacterized functional crosstalk responsible for RNAPII activity on damaged sites.

Last, MDC1's role in transcription may help human cells to cope with transcriptional stress. Here, we show that cancer cells lacking MDC1 are more sensitive to THZ1, a small-molecule inhibitor of CDK7,[59] compared with the normal counterparts (Figures 7E and S7A). Albeit limited at this stage, our data support the concept of cancer cells' dependency on particular transcription programs, responsible for the maintenance of their oncogenic state,[68,69] highlighting the emerging relevance of transcription inhibitors as promising therapeutic agents in oncology.[70] To date, CDK7 inhibition has been effectively used to treat lung and breast carcinomas.[71,72] Intriguingly, MDC1 is

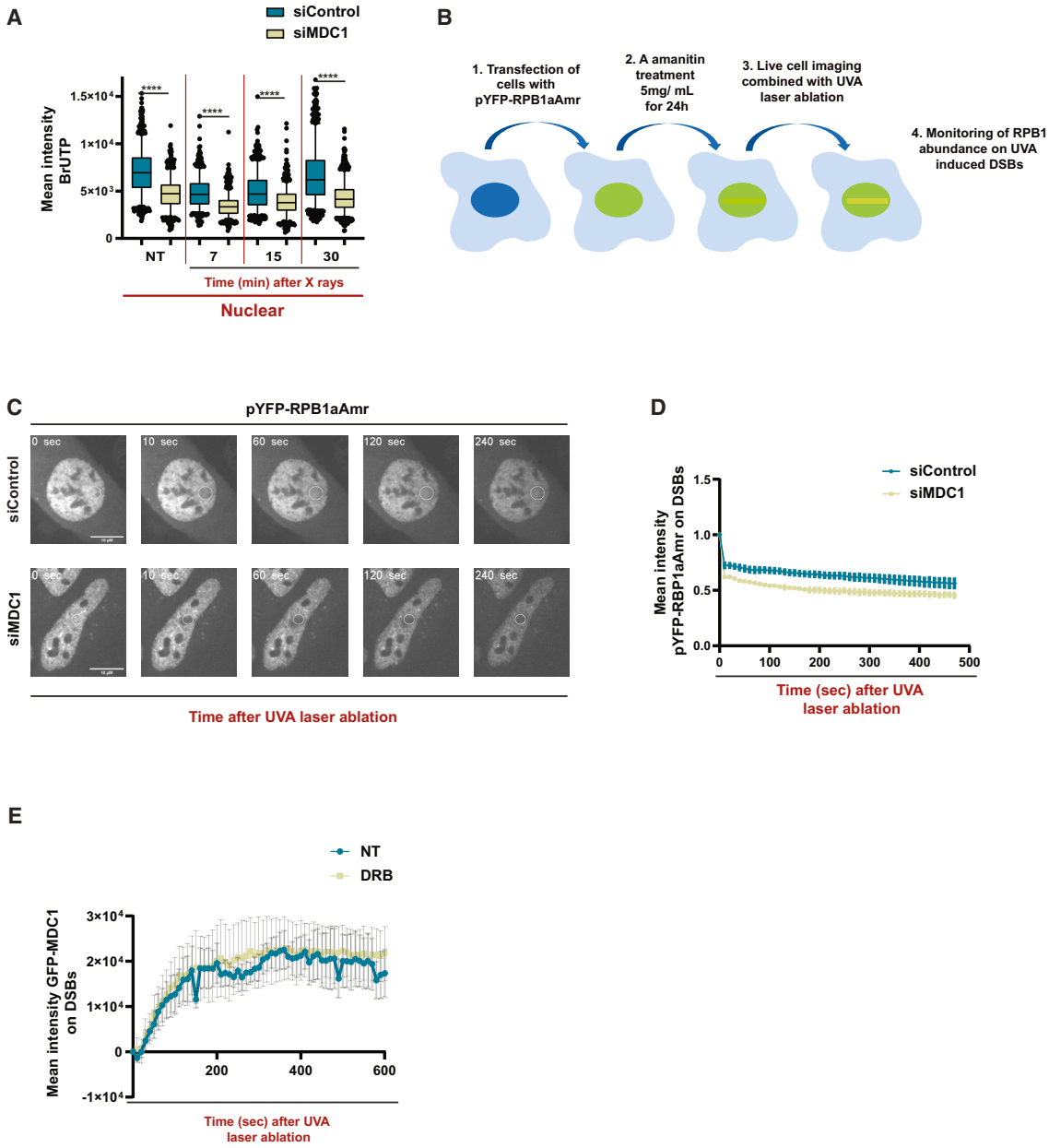

Figure 6. MDC1 depletion impairs the engagement of RNAPII on DSBs

(A) Relative quantification of nascent RNA synthesis in U2OS cells transfected with the indicated siRNAs following X irradiation (X-rays) (number of cells: n > 150). Individual values have been pooled together, and data are represented as mean ± SEM.

(B) Schematic representation of pYFP-RPB1aAmr U2OS cells subjected to live cell imaging experiment combined with UVA laser ablation to monitor alterations of RNAPII abundance on DSBs.

(C) Representative time-lapse images acquired from U2OS cells overexpressing pYFP-RPB1aAmr, transfected with the indicated siRNAs. DSBs formed are indicated by the white circle. Scale bars represent 10 μm.

(D) Relative quantification of the amount of the engaged YFP-RPB1 complexes on DSB sites (first 500 s following DSB formation) (number of cells: n > 10). Individual values have been pooled together, and data are represented as mean ± SEM.

(E) Relative quantification of EGFP-MDC1 early recruitment kinetics on DSB sites (first 600 s following DSB formation) upon DRB treatment. U2OS cells were transiently transfected with pEGFP-C2-MDC1 plasmids (number of cells: n > 10). Individual values have been pooled together, and data are represented as mean ± SEM.

****p < 0.0001, by unpaired Student's t test.

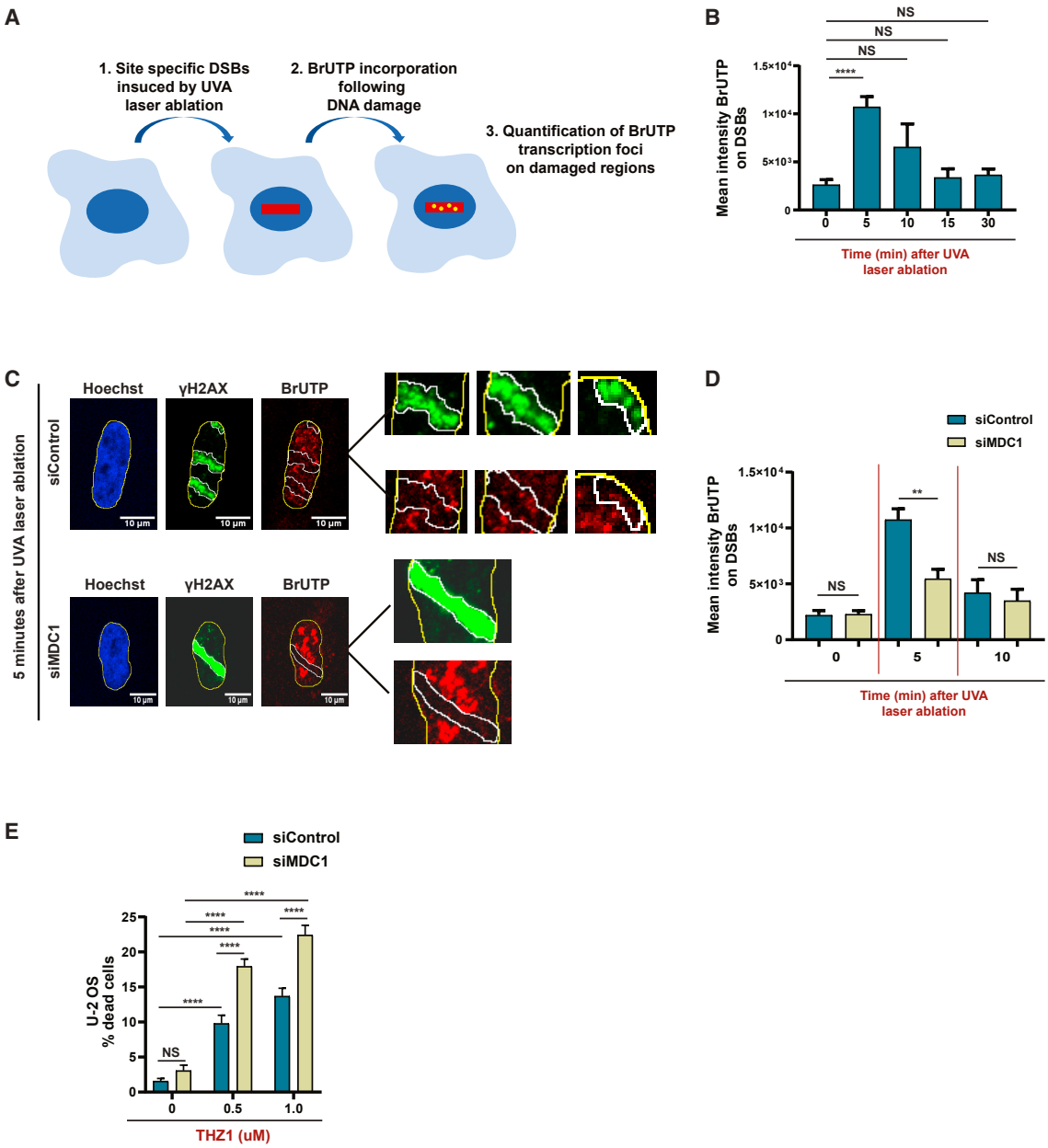

Figure 7. MDC1 knockdown impairs the de novo transcription on DSBs and sensitizes cells to THZ1 inhibitor

(A and B) Schematic representation of UVA laser ablation followed by BrUTP incorporation assay. BrUTP incorporation on DSBs (marked by γH2AX) was quantified at the indicated time points following damage (number of cells irradiated: n > 20). Individual values have been pooled together, and data are represented as mean ± SEM.

(C) Representative images of U2OS cells transfected with the indicated siRNAs, exposed to UVA laser microirradiation and incubated for 5 min. Cells were supplemented with BrUTP analog for an additional 8 min. Scale bars represent 10 μm.

(D) Quantification of nascent transcription on DSB sites on the basis of BrUTP incorporation upon transfection of the cells with the indicated siRNAs (number of biological replicates: n = 3). Biological replicates have been pooled together, and data are represented as mean ± SEM.

(E) Quantification of percentage dead cells following treatment with THZ1 inhibitor upon transfection with the indicated siRNAs (number of biological replicates: n = 4). Biological replicates have been pooled together, and data are represented as mean ± SEM.

NS, not significant; **p < 0.01; ****p < 0.0001, by unpaired Student's t test.

found to be downregulated in several cancers including breast and lung carcinomas (Figure S7F),[73,74] suggesting a potential predictive value of MDC1 abundance in selecting subsets of cancer patients for treatment with transcription inhibitors. Furthermore, MDC1 is known to play a central role in DDR, influencing the response of cancer cells to radiation and

DNA-damaging chemotherapeutics.[75,76] Taken together with the accumulating evidence in the field, the present findings may inspire more studies of potential synthetic lethal combinations of transcription inhibitors with DNA damaging agents, particularly in subsets of cancer patients with specific DDR defects, such as MDC1 deficiency examined here.

Limitations of the study

Despite the insights into the role of MDC1 in transcription and splicing, our present dataset cannot conclusively discriminate among the possible mechanistic causes of the observed lower RNAPII engagement in the absence of MDC1. Indeed, the mechanistic cause may include: (1) less loading of RNAPII on the DNA template, (2) increased promoter-proximal stalling, or (3) increased turnover of RNAPII complexes close to TSS. Moreover, particularly the present results related to enhanced sensitivity to THZ1-mediated transcription inhibition in human cancer cell line models depleted of MDC1 are limited and would benefit from supporting *in vivo* preclinical animal experiments or even clinical data.

STAR★METHODS

Detailed methods are provided in the online version of this paper and include the following:

- KEY RESOURCES TABLE
- RESOURCE AVAILABILITY
  - Lead contact
  - Materials availability
  - Data and code availability
- EXPERIMENTAL MODEL AND SUBJECT DETAILS
  - Cell lines
- METHOD DETAILS
  - Drugs and cell culture supplements
  - Plasmids and siRNAs transfections
  - Site-directed mutagenesis
  - MDC1 coding sequence (CDS)
  - Co-immunoprecipitation assay
  - Chromatin enriched fraction preparation/Western blot
  - Flow cytometry/EdU
  - BrUTP incorporation assay
  - EU Click-iT
  - Analysis of dead cell percentage
  - Indirect immunofluorescence (IF)
  - X irradiation (X-Rays)
  - UVA laser ablation using Nikon confocal microscope equipped with PerkinElmer spinning disk
  - UVA laser ablation_ P.A.L.M. Laser Technologies/ BrUTP incorporation assay
  - High-content microscopy and quantitative image-based cytometry (QIBC)
  - DRB-release-quantitative real-time PCR assay
  - Quantitative real-time PCR
  - RNA sequencing: Nanopore Sequencing Technologies
  - DRB/TT_{chem}-seq to measure RNAPII progression following release from DRB
- QUANTIFICATION AND STATISTICAL ANALYSIS

SUPPLEMENTAL INFORMATION

Supplemental information can be found online at https://doi.org/10.1016/j.celrep.2022.111979.

ACKNOWLEDGMENTS

We thank Dr. Junjie Chen for providing the HA-tagged MDC1 WT and deletion mutants (Figure 4A). We would like to thank Dr. Fabrizio d'Adda di Fagagna and Dr. Matteo Cabrini for the scientific discussions that improved the present study. J.B. and the members of his groups were funded by the European Union's Horizon 2020 research and innovation program under the Marie Skłodowska-Curie grant agreement 722729, by grants from the Danish Cancer Society (R167-A11068 and R204-A12617-B153), the Lundbeck Foundation (R266-2017-4289), the Novo Nordisk Foundation (NNF20OC0060590), the Swedish Research Council (VR-MH 2014-46602-117891-30), the Danish Council for Independent Research (DFF-7016-00313), and the Danish National Research Foundation (project CARD, DNRF 125). K.W. was supported by Japan Society for the Promotion of Science (JSPS) KAKENHI grants JP19K23927 and JP20K07578. P.G. is funded by a Lundbeck postdoctoral fellowship (R322-2019-2577). A.M.-M. was funded by the Danish Cancer Society (R302-A17590). D.H.L. and Z.G. were supported by the Danish Cancer Society, Danish Cancer Society-Knæk Cancer (R311-A18224), the Independent Research Fund Denmark (8045-00057A), and the Novo Nordisk Foundation (NNF18OC0052647). Work in the lab of L.H.G. is funded by a Hallas-Møller emerging investigator grant from the Novo Nordisk Foundation (NNF20OC0059959) and a Sapere Aude grant from Independent Research Fund Denmark (0165-00092B). Q.T. is funded by a Lundbeck postdoctoral fellowship (R380-2021-1284).

AUTHOR CONTRIBUTIONS

G.P., Z.G., H.H.G., D.G.-C., M.H.L., and P.G.: cell culture and manipulations, *in situ* transcription assay, EdU Click-iT assay, immunofluorescence analysis, immunoblots, qPCR, QIBC analysis, fluorescence-activated cell sorting (FACS), live cell imaging experiments combined with UVA laser irradiation, PALM microirradiation, survival assays, biochemical assays (co-immunoprecipitation and chromatin fractionation); G.P., S.H.N.M., D.C.K., and P.O.-C: cDNA library preparation and bioinformatic analysis of nanopore RNA sequencing data and interpretation; Q.T. and L.H.G.: preparation and performance of DRB/TT_{chem}-seq, analysis and interpretation of the data acquired from the sequencing; G.P., S.H.N.M., K.W., D.H.L., L.H.G., A.M.-M., P.G., and J.B.: data analysis and interpretation and manuscript preparation. G.P., A.M.-M., P.G., and J.B.: experimental design, supervision and manuscript writing with input from all co-authors.

DECLARATION OF INTERESTS

The authors declare no competing interests.

Received: December 14, 2021
Revised: October 4, 2022
Accepted: December 23, 2022

REFERENCES

1. Jackson, S.P., and Bartek, J. (2009). The DNA-damage response in human biology and disease. Nature *461*, 1071–1078. https://doi.org/10.1038/nature08467.
2. Petrini, J.H.J., and Stracker, T.H. (2003). The cellular response to DNA double-strand breaks: defining the sensors and mediators. Trends Cell Biol. *13*, 458–462. https://doi.org/10.1016/s0962-8924(03)00170-3.
3. Ozaki, T., Nagase, T., Ichimiya, S., Seki, N., Ohiri, M., Nomura, N., Takada, N., Sakiyama, S., Weber, B.L., and Nakagawara, A. (2000). NFBD1/KIAA0170 is a novel nuclear transcriptional transactivator with BRCT domain. DNA Cell Biol. *19*, 475–485. https://doi.org/10.1089/10445490050128403.

4. Leresche, A., Wolf, V.J., and Gottesfeld, J.M. (1996). Repression of RNA polymerase II and III transcription during M phase of the cell cycle. Exp. Cell Res. *229*, 282–288. https://doi.org/10.1006/excr.1996.0373.

5. Cramer, P. (2019). Organization and regulation of gene transcription. Nature *573*, 45–54. https://doi.org/10.1038/s41586-019-1517-4.

6. Chen, F.X., Smith, E.R., and Shilatifard, A. (2018). Born to run: control of transcription elongation by RNA polymerase II. Nat. Rev. Mol. Cell Biol. *19*, 464–478. https://doi.org/10.1038/s41580-018-0010-5.

7. Harlen, K.M., and Churchman, L.S. (2017). The code and beyond: transcription regulation by the RNA polymerase II carboxy-terminal domain. Nat. Rev. Mol. Cell Biol. *18*, 263–273. https://doi.org/10.1038/nrm.2017.10.

8. Liu, X., Kraus, W.L., and Bai, X. (2015). Ready, pause, go: regulation of RNA polymerase II pausing and release by cellular signaling pathways. Trends Biochem. Sci. *40*, 516–525. https://doi.org/10.1016/j.tibs.2015.07.003.

9. Lanctôt, C., Cheutin, T., Cremer, M., Cavalli, G., and Cremer, T. (2007). Dynamic genome architecture in the nuclear space: regulation of gene expression in three dimensions. Nat. Rev. Genet. *8*, 104–115. https://doi.org/10.1038/nrg2041.

10. Muniz, L., Nicolas, E., and Trouche, D. (2021). RNA polymerase II speed: a key player in controlling and adapting transcriptome composition. EMBO J. *40*, e105740. https://doi.org/10.15252/embj.2020105740.

11. Noe Gonzalez, M., Blears, D., and Svejstrup, J.Q. (2021). Causes and consequences of RNA polymerase II stalling during transcript elongation. Nat. Rev. Mol. Cell Biol. *22*, 3–21. https://doi.org/10.1038/s41580-020-00308-8.

12. Proudfoot, N.J. (2016). Transcriptional termination in mammals: stopping the RNA polymerase II juggernaut. Science *352*, aad9926. https://doi.org/10.1126/science.aad9926.

13. Jonkers, I., and Lis, J.T. (2015). Getting up to speed with transcription elongation by RNA polymerase II. Nat. Rev. Mol. Cell Biol. *16*, 167–177. https://doi.org/10.1038/nrm3953.

14. Heidemann, M., Hintermair, C., Voß, K., and Eick, D. (2013). Dynamic phosphorylation patterns of RNA polymerase II CTD during transcription. Biochim. Biophys. Acta *1829*, 55–62. https://doi.org/10.1016/j.bbagrm.2012.08.013.

15. Fong, N., Kim, H., Zhou, Y., Ji, X., Qiu, J., Saldi, T., Diener, K., Jones, K., Fu, X.D., and Bentley, D.L. (2014). Pre-mRNA splicing is facilitated by an optimal RNA polymerase II elongation rate. Genes Dev. *28*, 2663–2676. https://doi.org/10.1101/gad.252106.114.

16. Matera, A.G., and Wang, Z. (2014). A day in the life of the spliceosome. Nat. Rev. Mol. Cell Biol. *15*, 108–121. https://doi.org/10.1038/nrm3742.

17. Nguyen, H.D., Leong, W.Y., Li, W., Reddy, P.N.G., Sullivan, J.D., Walter, M.J., Zou, L., and Graubert, T.A. (2018). Spliceosome mutations induce R loop-associated sensitivity to ATR inhibition in myelodysplastic syndromes. Cancer Res. *78*, 5363–5374. https://doi.org/10.1158/0008-5472.Can-17-3970.

18. Shanbhag, N.M., Rafalska-Metcalf, I.U., Balane-Bolivar, C., Janicki, S.M., and Greenberg, R.A. (2010). ATM-dependent chromatin changes silence transcription in cis to DNA double-strand breaks. Cell *141*, 970–981. https://doi.org/10.1016/j.cell.2010.04.038.

19. Bader, A.S., Hawley, B.R., Wilczynska, A., and Bushell, M. (2020). The roles of RNA in DNA double-strand break repair. Br. J. Cancer *122*, 613–623. https://doi.org/10.1038/s41416-019-0624-1.

20. Ohle, C., Tesorero, R., Schermann, G., Dobrev, N., Sinning, I., and Fischer, T. (2016). Transient RNA-DNA hybrids are required for efficient double-strand break repair. Cell *167*, 1001–1013.e7. https://doi.org/10.1016/j.cell.2016.10.001.

21. Caron, P., Pankotai, T., Wiegant, W.W., Tollenaere, M.A.X., Furst, A., Bonhomme, C., Helfricht, A., de Groot, A., Pastink, A., Vertegaal, A.C.O., et al. (2019). WWP2 ubiquitylates RNA polymerase II for DNA-PK-dependent transcription arrest and repair at DNA breaks. Genes Dev. *33*, 684–704. https://doi.org/10.1101/gad.321943.118.

22. Pankotai, T., Bonhomme, C., Chen, D., and Soutoglou, E. (2012). DNAPKcs-dependent arrest of RNA polymerase II transcription in the presence of DNA breaks. Nat. Struct. Mol. Biol. *19*, 276–282. https://doi.org/10.1038/nsmb.2224.

23. Michelini, F., Jalihal, A.P., Francia, S., Meers, C., Neeb, Z.T., Rossiello, F., Gioia, U., Aguado, J., Jones-Weinert, C., Luke, B., et al. (2018). From "cellular" RNA to "smart" RNA: multiple roles of RNA in genome stability and beyond. Chem. Rev. *118*, 4365–4403. https://doi.org/10.1021/acs.chemrev.7b00487.

24. Michelini, F., Pitchiaya, S., Vitelli, V., Sharma, S., Gioia, U., Pessina, F., Cabrini, M., Wang, Y., Capozzo, I., Iannelli, F., et al. (2017). Damage-induced lncRNAs control the DNA damage response through interaction with DDRNAs at individual double-strand breaks. Nat. Cell Biol. *19*, 1400–1411. https://doi.org/10.1038/ncb3643.

25. Sharma, S., Anand, R., Zhang, X., Francia, S., Michelini, F., Galbiati, A., Williams, H., Ronato, D.A., Masson, J.Y., Rothenberg, E., et al. (2021). MRE11-RAD50-NBS1 complex is sufficient to promote transcription by RNA polymerase II at double-strand breaks by melting DNA ends. Cell Rep. *34*, 108565. https://doi.org/10.1016/j.celrep.2020.108565.

26. Wansink, D.G., Schul, W., van der Kraan, I., van Steensel, B., van Driel, R., and de Jong, L. (1993). Fluorescent labeling of nascent RNA reveals transcription by RNA polymerase II in domains scattered throughout the nucleus. J. Cell Biol. *122*, 283–293. https://doi.org/10.1083/jcb.122.2.283.

27. Dundr, M., Hoffmann-Rohrer, U., Hu, Q., Grummt, I., Rothblum, L.I., Phair, R.D., and Misteli, T. (2002). A kinetic framework for a mammalian RNA polymerase in vivo. Science *298*, 1623–1626. https://doi.org/10.1126/science.1076164.

28. Marzluff, W.F., Jr. (1978). Transcription of RNA in isolated nuclei. Methods Cell Biol. *19*, 317–332. https://doi.org/10.1016/s0091-679x(08)60032-1.

29. Li, B.B., Wang, B., Zhu, C.M., Tang, D., Pang, J., Zhao, J., Sun, C.H., Qiu, M.J., and Qian, Z.R. (2019). Cyclin-dependent kinase 7 inhibitor THZ1 in cancer therapy. Chronic Dis. Transl. Med. *5*, 155–169. https://doi.org/10.1016/j.cdtm.2019.08.006.

30. Chodosh, L.A., Fire, A., Samuels, M., and Sharp, P.A. (1989). 5,6-Dichloro-1-beta-D-ribofuranosylbenzimidazole inhibits transcription elongation by RNA polymerase II in vitro. J. Biol. Chem. *264*, 2250–2257.

31. Toledo, L.I., Altmeyer, M., Rask, M.B., Lukas, C., Larsen, D.H., Povlsen, L.K., Bekker-Jensen, S., Mailand, N., Bartek, J., and Lukas, J. (2013). ATR prohibits replication catastrophe by preventing global exhaustion of RPA. Cell *155*, 1088–1103. https://doi.org/10.1016/j.cell.2013.10.043.

32. Mailand, N., Bekker-Jensen, S., Faustrup, H., Melander, F., Bartek, J., Lukas, C., and Lukas, J. (2007). RNF8 ubiquitylates histones at DNA double-strand breaks and promotes assembly of repair proteins. Cell *131*, 887–900. https://doi.org/10.1016/j.cell.2007.09.040.

33. Lee, M.S., Edwards, R.A., Thede, G.L., and Glover, J.N.M. (2005). Structure of the BRCT repeat domain of MDC1 and its specificity for the free COOH-terminal end of the gamma-H2AX histone tail. J. Biol. Chem. *280*, 32053–32056. https://doi.org/10.1074/jbc.C500273200.

34. Wu, L., Luo, K., Lou, Z., and Chen, J. (2008). MDC1 regulates intra-S-phase checkpoint by targeting NBS1 to DNA double-strand breaks. Proc. Natl. Acad. Sci. USA *105*, 11200–11205. https://doi.org/10.1073/pnas.0802885105.

35. Kolas, N.K., Chapman, J.R., Nakada, S., Ylanko, J., Chahwan, R., Sweeney, F.D., Panier, S., Mendez, M., Wildenhain, J., Thomson, T.M., et al. (2007). Orchestration of the DNA-damage response by the RNF8 ubiquitin ligase. Science *318*, 1637–1640. https://doi.org/10.1126/science.1150034.

36. Jungmichel, S., and Stucki, M. (2010). MDC1: the art of keeping things in focus. Chromosoma *119*, 337–349. https://doi.org/10.1007/s00412-010-0266-9.

37. Coster, G., Hayouka, Z., Argaman, L., Strauss, C., Friedler, A., Brandeis, M., and Goldberg, M. (2007). The DNA damage response mediator MDC1 directly interacts with the anaphase-promoting complex/cyclosome. J. Biol. Chem. *282*, 32053–32064. https://doi.org/10.1074/jbc.M705890200.

38. Townsend, K., Mason, H., Blackford, A.N., Miller, E.S., Chapman, J.R., Sedgwick, G.G., Barone, G., Turnell, A.S., and Stewart, G.S. (2009). Mediator of DNA damage checkpoint 1 (MDC1) regulates mitotic progression. J. Biol. Chem. *284*, 33939–33948. https://doi.org/10.1074/jbc.M109.009191.

39. Leimbacher, P.A., Jones, S.E., Shorrocks, A.M.K., de Marco Zompit, M., Day, M., Blaauwendraad, J., Bundschuh, D., Bonham, S., Fischer, R., Fink, D., et al. (2019). MDC1 interacts with TOPBP1 to maintain chromosomal stability during mitosis. Mol. Cell *74*, 571–583.e8. https://doi.org/10.1016/j.molcel.2019.02.014.

40. Eliezer, Y., Argaman, L., Rhie, A., Doherty, A.J., and Goldberg, M. (2009). The direct interaction between 53BP1 and MDC1 is required for the recruitment of 53BP1 to sites of damage. J. Biol. Chem. *284*, 426–435. https://doi.org/10.1074/jbc.M807375200.

41. Lukas, C., Melander, F., Stucki, M., Falck, J., Bekker-Jensen, S., Goldberg, M., Lerenthal, Y., Jackson, S.P., Bartek, J., and Lukas, J. (2004). Mdc1 couples DNA double-strand break recognition by Nbs1 with its H2AX-dependent chromatin retention. EMBO J. *23*, 2674–2683. https://doi.org/10.1038/sj.emboj.7600269.

42. Wong, K.H., Jin, Y., and Struhl, K. (2014). TFIIH phosphorylation of the Pol II CTD stimulates mediator dissociation from the preinitiation complex and promoter escape. Mol. Cell *54*, 601–612. https://doi.org/10.1016/j.molcel.2014.03.024.

43. Jeronimo, C., and Robert, F. (2014). Kin28 regulates the transient association of Mediator with core promoters. Nat. Struct. Mol. Biol. *21*, 449–455. https://doi.org/10.1038/nsmb.2810.

44. Price, D.H. (2000). P-TEFb, a cyclin-dependent kinase controlling elongation by RNA polymerase II. Mol. Cell Biol. *20*, 2629–2634. https://doi.org/10.1128/mcb.20.8.2629-2634.2000.

45. Singh, J., and Padgett, R.A. (2009). Rates of in situ transcription and splicing in large human genes. Nat. Struct. Mol. Biol. *16*, 1128–1133. https://doi.org/10.1038/nsmb.1666.

46. Yamaguchi, Y., Takagi, T., Wada, T., Yano, K., Furuya, A., Sugimoto, S., Hasegawa, J., and Handa, H. (1999). NELF, a multisubunit complex containing RD, cooperates with DSIF to repress RNA polymerase II elongation. Cell *97*, 41–51. https://doi.org/10.1016/s0092-8674(00)80713-8.

47. Gregersen, L.H., Mitter, R., and Svejstrup, J.Q. (2020). Using TT(chem)-seq for profiling nascent transcription and measuring transcript elongation. Nat. Protoc. *15*, 604–627. https://doi.org/10.1038/s41596-019-0262-3.

48. Nojima, T., Gomes, T., Grosso, A.R.F., Kimura, H., Dye, M.J., Dhir, S., Carmo-Fonseca, M., and Proudfoot, N.J. (2015). Mammalian NET-seq reveals genome-wide nascent transcription coupled to RNA processing. Cell *161*, 526–540. https://doi.org/10.1016/j.cell.2015.03.027.

49. Gu, B., Eick, D., and Bensaude, O. (2013). CTD serine-2 plays a critical role in splicing and termination factor recruitment to RNA polymerase II in vivo. Nucleic Acids Res. *41*, 1591–1603. https://doi.org/10.1093/nar/gks1327.

50. Mayer, A., di Iulio, J., Maleri, S., Eser, U., Vierstra, J., Reynolds, A., Sandstrom, R., Stamatoyannopoulos, J.A., and Churchman, L.S. (2015). Native elongating transcript sequencing reveals human transcriptional activity at nucleotide resolution. Cell *161*, 541–554. https://doi.org/10.1016/j.cell.2015.03.010.

51. Oesterreich, F.C., Herzel, L., Straube, K., Hujer, K., Howard, J., and Neugebauer, K.M. (2016). Splicing of nascent RNA coincides with intron exit from RNA polymerase II. Cell *165*, 372–381. https://doi.org/10.1016/j.cell.2016.02.045.

52. Chanarat, S., and Sträßer, K. (2013). Splicing and beyond: the many faces of the Prp19 complex. Biochim. Biophys. Acta *1833*, 2126–2134. https://doi.org/10.1016/j.bbamcr.2013.05.023.

53. Tresini, M., Warmerdam, D.O., Kolovos, P., Snijder, L., Vrouwe, M.G., Demmers, J.A.A., van IJcken, W.F.J., Grosveld, F.G., Medema, R.H., Hoeijmakers, J.H.J., et al. (2015). The core spliceosome as target and effector of non-canonical ATM signalling. Nature *523*, 53–58. https://doi.org/10.1038/nature14512.

54. Herzel, L., Ottoz, D.S.M., Alpert, T., and Neugebauer, K.M. (2017). Splicing and transcription touch base: co-transcriptional spliceosome assembly and function. Nat. Rev. Mol. Cell Biol. *18*, 637–650. https://doi.org/10.1038/nrm.2017.63.

55. Kotake, Y., Sagane, K., Owa, T., Mimori-Kiyosue, Y., Shimizu, H., Uesugi, M., Ishihama, Y., Iwata, M., and Mizui, Y. (2007). Splicing factor SF3b as a target of the antitumor natural product pladienolide. Nat. Chem. Biol. *3*, 570–575. https://doi.org/10.1038/nchembio.2007.16.

56. Tang, A.D., Soulette, C.M., van Baren, M.J., Hart, K., Hrabeta-Robinson, E., Wu, C.J., and Brooks, A.N. (2020). Full-length transcript characterization of SF3B1 mutation in chronic lymphocytic leukemia reveals downregulation of retained introns. Nat. Commun. *11*, 1438. https://doi.org/10.1038/s41467-020-15171-6.

57. Francia, S., Cabrini, M., Matti, V., Oldani, A., and d'Adda di Fagagna, F. (2016). DICER, DROSHA and DNA damage response RNAs are necessary for the secondary recruitment of DNA damage response factors. J. Cell Sci. *129*, 1468–1476. https://doi.org/10.1242/jcs.182188.

58. Pessina, F., Giavazzi, F., Yin, Y., Gioia, U., Vitelli, V., Galbiati, A., Barozzi, S., Garre, M., Oldani, A., Flaus, A., et al. (2019). Functional transcription promoters at DNA double-strand breaks mediate RNA-driven phase separation of damage-response factors. Nat. Cell Biol. *21*, 1286–1299. https://doi.org/10.1038/s41556-019-0392-4.

59. Kwiatkowski, N., Zhang, T., Rahl, P.B., Abraham, B.J., Reddy, J., Ficarro, S.B., Dastur, A., Amzallag, A., Ramaswamy, S., Tesar, B., et al. (2014). Targeting transcription regulation in cancer with a covalent CDK7 inhibitor. Nature *511*, 616–620. https://doi.org/10.1038/nature13393.

60. Bacon, C.W., Challa, A., Hyder, U., Shukla, A., Borkar, A.N., Bayo, J., Liu, J., Wu, S.Y., Chiang, C.M., Kutateladze, T.G., and D'Orso, I. (2020). KAP1 is a chromatin reader that couples steps of RNA polymerase II transcription to sustain oncogenic programs. Mol. Cell *78*, 1133–1151.e14. https://doi.org/10.1016/j.molcel.2020.04.024.

61. Bunch, H., Lawney, B.P., Lin, Y.F., Asaithamby, A., Murshid, A., Wang, Y.E., Chen, B.P.C., and Calderwood, S.K. (2015). Transcriptional elongation requires DNA break-induced signalling. Nat. Commun. *6*, 10191. https://doi.org/10.1038/ncomms10191.

62. Wang, C., Sun, H., Zou, R., Zhou, T., Wang, S., Sun, S., Tong, C., Luo, H., Li, Y., Li, Z., et al. (2015). MDC1 functionally identified as an androgen receptor co-activator participates in suppression of prostate cancer. Nucleic Acids Res. *43*, 4893–4908. https://doi.org/10.1093/nar/gkv394.

63. Zou, R., Zhong, X., Wang, C., Sun, H., Wang, S., Lin, L., Sun, S., Tong, C., Luo, H., Gao, P., et al. (2015). MDC1 enhances estrogen receptor-mediated transactivation and contributes to breast cancer suppression. Int. J. Biol. Sci. *11*, 992–1005. https://doi.org/10.7150/ijbs.10918.

64. Salifou, K., Burnard, C., Basavarajaiah, P., Grasso, G., Helsmoortel, M., Mac, V., Depierre, D., Franckhauser, C., Beyne, E., Contreras, X., et al. (2021). Chromatin-associated MRN complex protects highly transcribing genes from genomic instability. Sci. Adv. *7*, eabb2947. https://doi.org/10.1126/sciadv.abb2947.

65. Chanarat, S., Seizl, M., and Strässer, K. (2011). The Prp19 complex is a novel transcription elongation factor required for TREX occupancy at transcribed genes. Genes Dev. *25*, 1147–1158. https://doi.org/10.1101/gad.623411.

66. Melander, F., Bekker-Jensen, S., Falck, J., Bartek, J., Mailand, N., and Lukas, J. (2008). Phosphorylation of SDT repeats in the MDC1 N terminus triggers retention of NBS1 at the DNA damage-modified chromatin. J. Cell Biol. *181*, 213–226. https://doi.org/10.1083/jcb.200708210.

67. Chapman, J.R., and Jackson, S.P. (2008). Phospho-dependent interactions between NBS1 and MDC1 mediate chromatin retention of the MRN complex at sites of DNA damage. EMBO Rep. *9*, 795–801. https://doi.org/10.1038/embor.2008.103.

68. Hnisz, D., Abraham, B.J., Lee, T.I., Lau, A., Saint-André, V., Sigova, A.A., Hoke, H.A., and Young, R.A. (2013). Super-enhancers in the control of cell identity and disease. Cell *155*, 934–947. https://doi.org/10.1016/j.cell.2013.09.053.

69. Bradner, J.E., Hnisz, D., and Young, R.A. (2017). Transcriptional addiction in cancer. Cell *168*, 629–643. https://doi.org/10.1016/j.cell.2016.12.013.

70. Sava, G.P., Fan, H., Coombes, R.C., Buluwela, L., and Ali, S. (2020). CDK7 inhibitors as anticancer drugs. Cancer Metastasis Rev. *39*, 805–823. https://doi.org/10.1007/s10555-020-09885-8.

71. Christensen, C.L., Kwiatkowski, N., Abraham, B.J., Carretero, J., Al-Shahrour, F., Zhang, T., Chipumuro, E., Herter-Sprie, G.S., Akbay, E.A., Altabef, A., et al. (2014). Targeting transcriptional addictions in small cell lung cancer with a covalent CDK7 inhibitor. Cancer Cell *26*, 909–922. https://doi.org/10.1016/j.ccell.2014.10.019.

72. Wang, Y., Zhang, T., Kwiatkowski, N., Abraham, B.J., Lee, T.I., Xie, S., Yuzugullu, H., Von, T., Li, H., Lin, Z., et al. (2015). CDK7-dependent transcriptional addiction in triple-negative breast cancer. Cell *163*, 174–186. https://doi.org/10.1016/j.cell.2015.08.063.

73. Bartkova, J., Horejsí, Z., Sehested, M., Nesland, J.M., Rajpert-De Meyts, E., Skakkebaek, N.E., Stucki, M., Jackson, S., Lukas, J., and Bartek, J. (2007). DNA damage response mediators MDC1 and 53BP1: constitutive activation and aberrant loss in breast and lung cancer, but not in testicular germ cell tumours. Oncogene *26*, 7414–7422. https://doi.org/10.1038/sj.onc.1210553.

74. Ruff, S.E., Logan, S.K., Garabedian, M.J., and Huang, T.T. (2020). Roles for MDC1 in cancer development and treatment. DNA Repair *95*, 102948. https://doi.org/10.1016/j.dnarep.2020.102948.

75. Nakanishi, M., Ozaki, T., Yamamoto, H., Hanamoto, T., Kikuchi, H., Furuya, K., Asaka, M., Delia, D., and Nakagawara, A. (2007). NFBD1/MDC1 associates with p53 and regulates its function at the crossroad between cell survival and death in response to DNA damage. J. Biol. Chem. *282*, 22993–23004. https://doi.org/10.1074/jbc.M611412200.

76. Peng, A., and Chen, P.L. (2003). NFBD1, like 53BP1, is an early and redundant transducer mediating Chk2 phosphorylation in response to DNA damage. J. Biol. Chem. *278*, 8873–8876. https://doi.org/10.1074/jbc.C300001200.

77. Darzacq, X., Shav-Tal, Y., de Turris, V., Brody, Y., Shenoy, S.M., Phair, R.D., and Singer, R.H. (2007). In vivo dynamics of RNA polymerase II transcription. Nat. Struct. Mol. Biol. *14*, 796–806. https://doi.org/10.1038/nsmb1280.

78. Shang, Y.L., Bodero, A.J., and Chen, P.L. (2003). NFBD1, a novel nuclear protein with signature motifs of FHA and BRCT, and an internal 41-amino acid repeat sequence, is an early participant in DNA damage response. J. Biol. Chem. *278*, 6323–6329. https://doi.org/10.1074/jbc.M210749200.

79. Uphoff, C.C., and Drexler, H.G. (2011). Detecting mycoplasma contamination in cell cultures by polymerase chain reaction. Methods Mol. Biol. *731*, 93–103. https://doi.org/10.1007/978-1-61779-080-5_8.

80. Liu, S., Hua, Y., Wang, J., Li, L., Yuan, J., Zhang, B., Wang, Z., Ji, J., and Kong, D. (2021). RNA polymerase III is required for the repair of DNA double-strand breaks by homologous recombination. Cell *184*, 1314–1329.e10. https://doi.org/10.1016/j.cell.2021.01.048.

81. De Coster, W., D'Hert, S., Schultz, D.T., Cruts, M., and Van Broeckhoven, C. (2018). NanoPack: visualizing and processing long-read sequencing data. Bioinformatics *34*, 2666–2669. https://doi.org/10.1093/bioinformatics/bty149.

82. Love, M.I., Huber, W., and Anders, S. (2014). Moderated estimation of fold change and dispersion for RNA-seq data with DESeq2. Genome Biol. *15*, 550. https://doi.org/10.1186/s13059-014-0550-8.

83. Dobin, A., Davis, C.A., Schlesinger, F., Drenkow, J., Zaleski, C., Jha, S., Batut, P., Chaisson, M., and Gingeras, T.R. (2013). STAR: ultrafast universal RNA-seq aligner. Bioinformatics *29*, 15–21. https://doi.org/10.1093/bioinformatics/bts635.

84. Smith, T., Heger, A., and Sudbery, I. (2017). UMI-tools: modeling sequencing errors in Unique Molecular Identifiers to improve quantification accuracy. Genome Res. *27*, 491–499. https://doi.org/10.1101/gr.209601.116.

85. Quinlan, A.R., and Hall, I.M. (2010). BEDTools: a flexible suite of utilities for comparing genomic features. Bioinformatics *26*, 841–842. https://doi.org/10.1093/bioinformatics/btq033.

86. Gregersen, L.H., Mitter, R., Ugalde, A.P., Nojima, T., Proudfoot, N.J., Agami, R., Stewart, A., and Svejstrup, J.Q. (2019). SCAF4 and SCAF8, mRNA anti-terminator proteins. Cell *177*, 1797–1813.e18. https://doi.org/10.1016/j.cell.2019.04.038.

STAR★METHODS

KEY RESOURCES TABLE

REAGENT or RESOURCE	SOURCE	IDENTIFIER
Antibodies		
Mouse anti- BrdU (pure B44 100T)	BD Biosciences	Cat#347580; RRID: AB_10015219
Rat anti-BrdU	AbD serotec	Cat#OBT0030; RRID: AB_609568
Rabbit polyclonal anti- MDC1	Abcam	Cat#ab11171; RRID: AB_297810
Mouse monoclonal anti-RNAPII	Abcam	Cat#ab817; RRID: AB_306327
Mouse monoclonal anti- POLR2A	NeoBiotech	Cat#NB-01-0110
Rabbit polyclonal anti- RNAPII (pSer2)	Abcam	Cat#ab5095; RRID: AB_304749
Rabbit polyclonal anti- RNAPII (pSer5)	Abcam	Cat#ab5131; RRID: AB_449369
Rat monoclonal anti- RNAPII (pSer2) 3E10	Sigma	Cat#04-1571; RRID: AB_11212363
Rat monoclonal anti- RNAPII (pSer5) 3E8	Sigma	Cat#04-1572; RRID: AB_10615822
Rabbit polyclonal anti- PLRG1	Bethyl Laboratories	Cat#A301-940A; RRID: AB_1548014
Mouse monoclonal anti- CDC5L	BD Biosciences	Cat#612362; RRID: AB_399724
Mouse monoclonal anti- PRP8	Santa Cruz	Cat#sc-55533; RRID: AB_831685
Rabbit polyclonal anti- SF3B3	Abcam	Cat#ab96683; RRID: AB_10648871
Rabbit polyclonal anti- SF3B2	Novus	Cat#NB100-79847; RRID: AB_1110397
Mouse monoclonal anti- H2A.X (pS140)	Abcam	Cat#ab22551; RRID: AB_447150
Rabbit polyclonal anti- H2A.X (pS139)	Cell Signaling	Cat#2577S; RRID: AB_2118010
Rabbit polyclonal anti- 53BP1	Abcam	Cat#ab36823; RRID: AB_722497
Rabbit polyclonal anti- H3	Abcam	Cat#ab1791; RRID: AB_302613
HA tag monoclonal antibody	Invitrogen	Cat#26183; RRID: AB_2610625
Mouse monoclonal anti- A tubulin	Gene Tex	Cat#GTX628802; RRID: AB_2716636
Mouse monoclonal anti-Vinculin	Sigma	Cat#V9131; RRID: AB_477629
Alexa Fluor™ 568 Goat anti-mouse	Invitrogen	Cat#A-11031; RRID: AB_144696
Alexa Fluor™ 488 Goat anti-rabbit	Invitrogen	Cat#A-11034; RRID: AB_2576217
Alexa Fluor™ 488 Goat anti-mouse	Invitrogen	Cat#A-11029; RRID: AB_2534088
Alexa Fluor™ 647 Goat anti-rabbit	Invitrogen	Cat#A-21245; RRID: AB_2535813
Goat anti-rat IgG (H + L) Cross-absorbed secondary antibody, DyLight 555	Invitrogen	Cat#A-21434; RRID: AB_141733
Horse anti-mouse IgG (H+L) Peroxidase	Vector laboratories	Cat#PI-2000; RRID: AB_2336177
Goat anti-rabbit IgG (H + L) Peroxidase	Vector laboratories	Cat#PI-1000; RRID: AB_2336198
Rabbit anti-rat IgG (H + L) secondary antibody HRP conjugate	Invitrogen	Cat#61-9520; RRID: AB_2533945
TrueBlot Ultra anti-mouse IgG HRP	eBioscience	Cat#18-8817; RRID: AB_10146399
TrueBlot Ultra anti-mouse IgG HRP	Rockland	Cat#18-8816-33; RRID: AB_469529
Bacterial and virus strains		
One Shot™ TOP10 Chemically Competent E. coli	Thermo Fischer Scientific	Cat#C404010
One Shot® Max Efficiency® DH5α™-T1^R Cells	Thermo Fischer Scientific	Cat#A14604
Chemicals, peptides, and recombinant proteins		
Propidium Iodine (PI)	Thermo Fischer Scientific	Cat#P1304MP
5,6-Dichlorobenzimidazole 1-βD-ribofuranoside (DRB)	Sigma	Cat#D1916
5-Ethynyluridine (EU)	Thermo Fischer Scientific	Cat#E10345
α-Amanitin	Sigma	Cat#A2263

(*Continued on next page*)

Continued

REAGENT or RESOURCE	SOURCE	IDENTIFIER
THZ1	Calbiochem	Cat#532372
5-bromo-2-deoxyuridine (BrdU)	GE Healthcare	Cat#RPN 202
Hoechst 33342 Trihydrochloride, Trihydrate	Invitrogen	Cat#H3570
Vectashield	Vector laboratories	Cat#H1000
5-Bromouridine 5′-triphosphate sodium salt (BrUTP)	Sigma	Cat#B7166
Adenosine 5′-triphosphate (ATP) Lithium salt	Sigma	Cat#11140965001
Guanosine 5′-triphosphate (GTP) solution	Sigma	Cat#11140957001
Cytidine 5′-triphoshate (CTP) Lithium salt	Sigma	Cat#11140922001
RNase Inhibitor	Thermo Fisher Scientific	Cat#N8080119
Fast SYBR™ Green Master Mix	Thermo Fisher Scientific	Cat#4385612
dNTP Set (100mM)	Thermo Fisher Scientific	Cat#10297018
PhosSTOP™	Sigma	Cat#4906837001
cOmplete™, EDTA-free Protease Inhibitor cocktail	Sigma	Cat#04693132001
DMEM^{GFP}-2	Evrogen	Cat#MC-102
Gibco ™ DMEM, high glucose, GlutaMAX™ Supplement	Thermo Fisher Scientific	Cat#10566016
Keratinocyte-SFM Medium (Kit) with L-glutamine, EGF, and BPE	Thermo Fisher Scientific	Cat#17005075
CO_2 Independent Medium	Thermo Fisher Scientific	Cat#18045088
Fetal Bovine Serum	Thermo Fisher Scientific	Cat#10270106
Penicillin-Streptomycin	Thermo Fisher Scientific	Cat#15070063
TrypLE Express (1X) (500mL)	Thermo Fisher Scientific	Cat#12604-021
TRIzol™ Reagent	Invitrogen	Cat#15596026
4-Thiouridine	Biosynth Carbosynth	Cat#NT06186
4-Thiouracil	Sigma	Cat#440736
Biotin-XX MTSEA	Biotium	Cat#BT90066
NEBNext® Multiplex Oligos for Illumina®	New England BioLabs	Cat#E7416
Dynabeads™ Protein G	Thermo Fisher Scientific	Cat#10004D
ECL™ Western Blotting Reagents	VWR	Cat#RPN2106
LongAmp® Taq 2X Master Mix	New England BioLabs	Cat#M0287S
AccuPrime™ Pfx DNA Polymerase	Invitrogen	Cat#12344024
Pladienolide B inhibitor (PLAB)	TOCRIS	Cat#6070
Critical commercial assays		
EdU Click-iT Alexa 647	Thermo Fischer Scientific	Cat#C10340
Lipofectamine™ RNAiMAX transfections reagent	Invitrogen	Cat#13778150
Lipofectamine™ LTX Reagent with PLUS™ Regent	Invitrogen	Cat#15338100
High-Capacity cDNA Reverse Transcription Kit	Thermo Fisher Scientific	Cat#4368814
Click-iT™ EdU Cell Proliferation Kit for Imaging, Alexa Fluor™ 647 dye	Thermo Fisher Scientific	Cat#C10340
Nuclear Complex Co-IP Kit	Active Motif	Cat#54001
GeneArt™ Site-Directed Mutagenesis PLUS System	Invitrogen	Cat#A14604
Maxima H Minus Reverse Transcriptase (200 U/μL)	Thermo Fisher Scientific	Cat#EP0751
RNeasy Mini Kit	Qiagen	Cat#74004
NucleoBond Xtra Maxi Kit	Macherey-Nagel	Cat#740414.50
μMACS™ and MultiMACS™ Strepavidin Kits	Miltenyi Biotec	Cat#130-074-101
RNeasy MinElute Cleanup Kit	Qiagen	Cat#74204
NEBNext® Ultra II Directional RNA Library Prep Kit for Illumina®	New England BioLabs	Cat#E7760

(*Continued on next page*)

Continued

REAGENT or RESOURCE	SOURCE	IDENTIFIER
Click-iT™ RNA Alexa Fluor™ 594 Imaging Kit	Thermo Fisher Scientific	Cat#C10330
Deposited data		
Raw Western Blot	Mendeley	https://doi.org/10.17632/j3p84sb38k.1
DRB/TT$_{chem}$-seq data	This paper	GEO: GSE215990
Nanopore RNA sequencing data	This paper	ArrayExpress: E-MTAB-12497
Experimental models: Cell lines		
Human: Passage 15 U-2 OS	ATCC	Cat#HTB-96
Human: HeLa	ATCC	Cat#CCL-2
Human: HBEC-3KT	ATCC	Cat#CRL-4051
Human: hTERT RPE-1	ATCC	Cat#CRL-4000
Recombinant DNA		
pYFP-RPB1aAmr	Addgene; Darzacq X et al., 2007[77]	#75284
pcDNA3-HA MDC1 (WT)	Wu L., et al., 2008[34]	N/A
pcDNA3-HA MDC1 (ΔFHA)	Wu L., et al., 2008[34]	N/A
pcDNA3-HA MDC1 (ΔS/TQ)	Wu L., et al., 2008[34]	N/A
pcDNA3-HA MDC1 (ΔPST)	Wu L., et al., 2008[34]	N/A
pcDNA3-HA MDC1 (ΔSDTD)	Wu L., et al., 2008[34]	N/A
pcDNA3-HA MDC1 (ΔBRCT)	Wu L., et al., 2008[34]	N/A
pEGFP-C2-MDC1	Shang Y. L. et al., 2013[78]	N/A
Oligonucleotides		
MDC1 mut#1 Forward primer (5′-3′): GAGCAATCCAGTGAATCGCT GAGGTGTAACGTGGAG	This paper	N/A
MDC1 mut#1 Reverse primer (5′-3′): CTCCACGTTACACCTCAGCG ATTCACTGGATTGCTC	This paper	N/A
MDC1 mut#2 Forward primer (5′-3′): GCAATCCAGTGAATCGCTAC GGTGTAACGTGGAGCCAG	This paper	N/A
MDC1 mut#2 Reverse primer (5′-3′): CTGGCTCCACGTTACACCGT AGCGATTCACTGGATTGC	This paper	N/A
Software and algorithms		
Fiji (ImageJ)	NIH	N/A
GraphPad Prism 8	GraphPad	https://www.graphpad.com/scientificsoftware/prism/
TIBCO Spotfire	Perkin Elmer	https://perkinelmerinformatics.com/products/exclusive-reseller/tibco-spotfire
ScanR Acquisition software	Olympus	https://www.olympus-lifescience.com/en/microscopes/inverted/scanr/
ScanR Analysis software	Olympus	https://www.olympus-lifescience.com/en/microscopes/inverted/scanr/
ZEN (Blue Edition)	Zeiss	N/A
FlowJo	BD Biosciences	https://www.flowjo.com/solutions/flowjo/downloads/v9
Volocity software	PerkinElmer	https://www.volocity4d.com/

RESOURCE AVAILABILITY

Lead contact

Further information and requests for resources and reagents should be directed to and will be fulfilled by the Lead Contact, JB (JB@cancer.dk).

Materials availability

This study did not generate any new unique reagents.

Data and code availability

- Raw Western Blot from Figures 2A and 4B, S1B, S1C, S1E, S2J, S2E, S4A, S4B, S5A, S6A, and S6C have been deposited to Mendeley (https://doi.org/10.17632/j3p84sb38k.1) and are publicly available as of the day of publication. Microscopy data reported in the current research article will be shared by the lead contact upon request. RNA sequencing raw and processed data from DRB/TT$_{chem}$-seq have been deposited in GEO (GSE215990) and are publicly available as of the date of publication. Nanopore RNA sequencing raw data have been deposited in ArrayExpress (E-MTAB-12497) and are publicly available as of the date of publication. Processed data acquired via Nanopore sequencing will be shared by the lead contact upon request. Accession numbers are listed in the key resources table.
- This paper does not report original code.
- Any additional information required to reanalyze the data reported in this paper is available from the lead contact upon request.

EXPERIMENTAL MODEL AND SUBJECT DETAILS

Cell lines

U2OS osteosarcoma cancer cells (15-year-old female patient), HeLa cervical cancer cells (31-year-old female patient) and hTERT RPE-1 (ATCC) immortalized normal epithelial cells (1-year-old female child) of human origin were cultured in high-glucose Dulbecco's Modified Eagle Medium (DMEM) plus GlutaMax supplemented with 10% FBS, 100 μg/mL streptomycin and 100 U/mLL penicillin at 37°C and 5% CO_2. HBEC-3KT (ATCC) bronchial epithelial cells (65-year-old female patient) of human origin were cultured in keratinocyte serum-free medium (#17005-075, Invitrogen) supplemented with 50 μg/mL Bovine Pituitary Extract and 5 ng/mL hEGF (#17005-075, Invitrogen) at 37°C and 5% CO_2. Cell lines are authenticated by STR profiling (StemElite ID Systems, Promega). They have been also tested for mycoplasma contamination with PCR analysis.[79]

METHOD DETAILS

Drugs and cell culture supplements

U2OS cells were cultivated in DMEM^{GFP}-2 (MC-102, Evrogen) during live cell imaging experiment (combined with UVA laser ablation). Cells placed on P.A.L.M. microlaser workstation (P.A.L.M. Laser Technologies) were cultivated in CO_2 Independent Medium (listed in the resource table). U2OS cells were treated with 100μM of DRB inhibitor (Sigma) for 4 h in culture conditions (37°C and 5% CO_2). Release of cells from DRB reversible inhibition was carried out by the removal of DRB supplemented medium followed by 2 serial washes with PBS and the addition of fresh (DRB free) culture medium. PLAB inhibitor was added at a final concentration of 5nM in the culture medium and cells were incubated for 3 h in the presence of the inhibitor. Cells were UVC irradiated (30J/m^2) and incubated for 50 min at 37°C, 5%CO_2 prior to co-immunoprecipitation. A-amanitin was added to a final concentration of 5ng and cells were incubated for 24 h prior to live cell imaging experiment. U2OS cells were incubated with 10nM of BrdU in culture medium for 24 h prior to laser microirradiation (Chromatin pre-sensitization). U2OS cells were treated with THZ1 inhibitor 1.0μM for 1 h. U2OS and RPE-1 cells were incubated with THZ1 (0.5μM, 1.0μM) inhibitor for 48 h prior to the analysis of the percentage of dead cells.

Plasmids and siRNAs transfections

Plasmids pcDNA3-HA-MDC1 Wild Type (WT) and deletion mutants (ΔFHA, ΔSDTD, ΔS/TQ, ΔPST, ΔBRCTs) (Figure 1F) were obtained from Junjie Chen laboratory described previously.[34] Cells were transfected for 24 h with pcDNA3-HA-MDC1 plasmids prior to the experiment. pYFP-RPB1aAmr plasmid was purchased from Addgene (#75284). pEGFP-C2-MDC1 plasmid was obtained from Phang-Lang Chen laboratory.[78] Cells were incubated for 48 h following transfection with pYFP-RPB1aAmr and pEGFP-C2-MDC1 plasmids. Plasmid transfections were carried out by Lipofectamine LTX with plus reagent (Invitrogen, #15338100) according to the manufacturer's instructions. siRNAs were obtained from Eurofins Genomics and transfections were performed using lipofectamine RNAiMax mix reagent (Invitrogen, #13778150), according to the manufacturer's instructions (The sequences of siRNAs are listed in Table S2). Cells were incubated for 72 h following siRNA transfection in every experimental setup. Culture media were refreshed after 24 h following transfection reactions.

Site-directed mutagenesis

Site-directed mutagenesis on MDC1 WT and mutant plasmids (ΔFHA, ΔSDTD, ΔS/TQ, ΔPST, ΔBRCTs) was carried using ''GeneArt Site-Directed Mutagenesis PLUS kit'' (#A14604) to gain resistance against siMDC1 siRNA (5′-UCCAGUGAAUCCUUGAGGU-3′, listed in Table S2) according to manufacturer instructions. Pfx DNA polymerase was used for the amplification step due to its ability to amplify with high efficiency large DNA templates (up to 14kb) that was ideal for our experimental setup considering the size of the pcDNA3-HA-MDC1 plasmids (around 12kb). Two rounds of site-directed mutagenesis have been carried out resulting in a total number of 4 nucleotide substitutions in the coding sequence of MDC1 WT and deletion mutants with no subsequent alteration in the open reading frame (silent mutations). Two pairs of DNA oligos have been designed accordingly, carrying two altered nucleotides (point mutations) each.

MDC1 mut#1 oligos:

Forward: 5′- GAGCAATCCAGTGAATCGCTGAGGTGTAACGTGGAG**-3′**

Reverse: 5′- CTCCACGTTACACCTCAGCGATTCACTGGATTGCTC**-3′**

MDC1 mut#2 oligos:

Forward: 5′- GCAATCCAGTGAATCGCTACGGTGTAACGTGGAGCCAG**-3′**

Reverse: 5′- CTGGCTCCACGTTACACCGTAGCGATTCACTGGATTGC**-3′**

The siMDC1 siRNA used in our experiments is complementary to the highlighted sequence that exists close to the 5′ end of the MDC1 coding sequence detected in both the WT and deletion mutants.

MDC1 coding sequence (CDS)

The sequence of MDC1 CDS that is close to the 5′ end of the insert has been attached. siMDC1 siRNA targeted sequence is listed in Table S2, and the nucleotide substitutions are shown. C-T-G-A nucleotides (in bold and red color) have been replaced by G-C-A-C, respectively resulting in siRNA resistance (siMDC1) of the pcDNA3-HA-MDC1 plasmids both of the WT and the deletion mutants.

5′-ATGGAGGACACCCAGGCTATTGACTGGGATGTTGAAGAAGAGGAGGAGACAGAGCA.
ATCCAGTGAATCC^{G}T^{C}TG^{A}A^{C}GGTGTAACGTGGAGCCAGTAGGGCGGCTACATATCTTTA
GTGGTGCCCATGGACCAGAAAAAGATTTCCCACTACACCTCGGGAAGAATGTGGTAGG.
CCGAATGCCTGACTGCTCTGTG-3′

Sequencing of the mutant plasmids was performed by Eurofins Genomics private company using appropriate primers for sequencing (listed in Table S1).

Co-immunoprecipitation assay

U2OS nuclear protein fractions were prepared by using the Nuclear Complex co-IP kit (Active Motif #5400), according to the manufacturer. Nuclear extracts were processed with the enzymatic cocktail reagent included in the kit and nucleic acid digestion was carried out (via this kit, pure protein-protein interactions are studied once both DNA and RNA molecules are degraded before the immunoprecipitation). Samples were subsequently diluted in appropriate volume of IP buffer (0.5% NP40, 50mM Tris-HCl, pH 7.4, 150mM NaCl, 1mM EDTA) supplemented with protease and phosphatase inhibitors. Diluted nuclear extracts were incubated with specific antibodies against the different protein targets (listed in the resource table) overnight at 4°C. Protein extracts were then incubated with 25μL of protein G dynabeads (Thermo Fisher, 10004D) for 1 h at 4°C. Beads were washed 5 times with 250μL of IP buffer and 20μL of Laemmli sample buffer were added combined with heating at 97°C for 5 min to elute the precipitated protein fractions from the beads. Protein-protein interactions were analyzed via immunoblot. Semi-quantification of each protein-protein interactions (protein bands density) was calculated based on chemiluminescence and was normalized against inputs (10% input). Band densities were measured via Fiji (ImageJ).

Chromatin enriched fraction preparation/Western blot

Cells were washed once with cold PBS, and incubated with TNE extraction buffer (150mM NaCl, 50mM Tri-HCl pH 7.4, 1mM EDTA, 0.1% NP40) supplemented with phosphatase (PhoSTOP EASY pack, 4906837001, Sigma) and protease (Complete EDTA free protease inhibitor cocktail, 4693132001, Sigma) inhibitors for 10 min on ice. TNE buffer was then discarded, the cells were washed twice with PBS and incubated with Laemnli buffer (4% SDS, 20% glycerol and 125 mM Tris-HCl, pH 6.8). Proteins were resolved by SDS-PAGE and transferred to nitrocellulose membranes (IB3002, Invitrogen), followed by immunoblotting. Western blot analysis was carried out using the antibodies listed in the resource table.

Primary antibodies were diluted in 0.01% PBS-Tween 20 containing 5% milk and were incubated overnight at 4°C. Secondary peroxidase-coupled antibodies were diluted in 0.01% PBS-Tween 20 containing 5% milk and incubated for 1 h at Room Temperature (RT). Protein bands were detected via ECL-based chemiluminescence. Semi-quantification of the bands' density was carried out by Fiji (ImageJ) and the values were normalized against the band density of H3, used as our internal control/loading control.

Flow cytometry/EdU

Cells were incubated with 10μM of EdU Thymidine analog for 30 min at 37°C. Cells were incubated with TrypLE Express (#12604-021) and harvested and transferred in a 15mL falcon tube. They were centrifuged at 1000 rpm at RT for 4 min, supernatant was discarded, and cells were resuspended in 1mL of cold PBS. A second round of centrifugation was carried out at 1000 rpm at RT for 4 min, the

supernatant was discarded, and cells were resuspended in 300μL of cold PBS. 700μL of 99% of ethanol (Absolute Ethanol) were added in a drop-by-drop manner in the falcon tube under constant shaking (final concentration of ethanol reached 70%) and samples were kept at −20°C until the day of staining. Cells were centrifuged at 1000 rpm at RT for 4 min, the supernatant was discarded, and they were resuspended in 1mL of cold PBS and transferred to special FACS tubes. Next, they were centrifuged at 1000 rpm at RT, supernatant was discarded and 1mL of PBS + blocking buffer (PBS, 0.1% FBS, 0.05%NaN3) was added. An additional step of centrifugation with the same settings was performed, the supernatant was discarded and 100μL of Click-iT reaction buffer was added to the cell pellets. Click-iT chemistry was used for the detection of EdU (Thermo Fischer Scientific, #C10340), according to the manufacturer. Cells were incubated for 30 min at RT in the dark under constant shaking. Then, 2mL of PBS+ were added and cells were centrifuged at 1000 rpm for 5 min at RT and Hoechst (H33342) diluted in PBS (1:1000) was added. Cells were incubated for 30 min at RT in the dark, 2mL of PBS+ were added by the end of the incubation period and cells were centrifuged at 1000 rpm for 5 min at RT. After removal of the supernatant, 300 μL of PBS were added and cells were stored at 4°C until FACS was performed. The cell cycle profile was analyzed on FACSVerse (Becton, Dickinson) and acquired data were analyzed using Flowjo software (TreeStar) where gating for each cell cycle phase was carried out.

BrUTP incorporation assay

Reagents' preparation

Permeabilization buffer:		
Reagents	Total volume 0.5mL	Total volume 1mL
20mM Tris pH 7.4 (stock 1M)	10 μL	20μL
5mM MgCl2 (stock 50mM)	50μL	100μL
0.5mM EGTA (stock 0.5M)	0.5μL	1μL
25% Glycerol (stock 100%)	125μL	250μL
0.1% Triton X-100 (stock 20%)	2.5μL	5μL
1mM PMSF (stock 100mM)	5μL	10μL
RNase Inhibitor (stock 2000 units)	0.5μL	1μL
DdH2O	306.5μL	613μL

Transcription buffer:		
Reagents	Total volume 0.5mL	Total volume 1mL
100mM KCl (stock 1M)	50μL	100μL
50mM Tris pH 7.4 (stock 1M)	25μL	50μL
10mM MgCl2 (stock 50mM)	100μL	200μL
0.5mM EGTA (stock 0.5M)	0.5μL	1μL
25% Glycerol (stock 100%)	125μL	250μL
1mM PMSF (stock 100mM)	5μL	10μL
RNase Inhibitor (stock 2000 units)	0.5μL	1μL
DdH2O	186μL	372μL
1mM ATP (stock 100mM)	5μL	10μL
200nM CTP (stock 100mM)	1μL	2μL
200nM GTP (stock 100mM)	1μL	2μL
200nM BrUTP (stock 100mM)	1μL	2μL

Permeabilization and transcription buffers are gently mixed and transferred in the cell incubator (5% CO_2, 37°C) for at least 30 min.

BrUTP analog incorporation

Cells are seeded on autoclaved 12mm coverslips (631-0713, Menzel-Glaser) so that on the day of the 5-bromouridine-5′-triphosphate (BrUTP) incorporation assay the coverslips are 70–75% confluent. Coverslips were gently pressed toward the bottom of the plates prior to the seeding to get an even distribution of the cells. Coverslips were washed once with warm PBS and were incubated with the permeabilization buffer for 2 min at RT. During the step of permeabilization, non-engaged RNAPII complexes are removed so that only the engaged ones are triggered to incorporate the BrUTP analog. Aspiration of the permeabilization buffer was followed by the addition of the transcription buffer and coverslips were incubated at 37°C, 5% CO_2 for 8 min. Then, the coverslips

were washed once with cold PBS and fixed with 4% Formaldehyde solution (listed in the resource table) for 15 min at RT. Coverslips were kept in the refrigerator in PBS until the staining procedure. The main advantage of the BrUTP incorporation assay is that it reveals an immediate snapshot of the transcription landscape of the cells compared to the widely used 5′ethynyluridine (EU) Click-iT reaction, where the incubation time with the EU analog is approximately 30 min.

Image acquisition and analysis of BrUTP incorporation

Image acquisition was carried out through point scanning confocal microscope LSM800 (Zeiss) using 63x oil immersion objective and ZEN software (Zeiss). Quantifications of the signal mean intensity in either nucleus (with subtracted nucleoli) or nucleoli were performed via ZEN blue software (Zeiss). Quantification of the total nuclear (both nucleolar and nuclear signal with subtracted nucleoli) BrUTP incorporation was carried out in an automated manner via Fiji (ImageJ) using Hoechst nuclear DNA staining as a mask. More than 150 cells were analyzed per biological replicate and average signal intensity was calculated per replicate in each condition. Values were normalized to the siControl samples of each experimental condition, or individual values of BrUTP signal intensity were plotted.

EU Click-iT

Cells are seeded on autoclaved 12mm coverslips (631-0713, Menzel-Glaser) so that the day of the 5-Ethynyluridine (EU) treatment the coverslips are 70–75% confluent. Cells were treated with 1mM EU for 30 min in cell culture conditions (37°C, 5% CO_2). Coverslips were washed once with cold PBS and fixed with 4% Formaldehyde solution (listed in the resource table) for 15 min in RT. Formaldehyde solution was discarded and cold PBS was added, and coverslips were stored at 4°C until the staining process. *In situ* detection of newly synthesized RNAs was carried out based in Click-iT chemical reaction using Click-iT RNA Alexa Fluor 594 Imaging Kit (Invitrogen, Molecular Probes #C10330), according to manufacturer's recommendations. Signal quantification was performed in an automated way via high-content microscopy and quantitative image-based cytometry (QIBC) described below. Values were normalized to the siControl samples of each experimental conditions.

Analysis of dead cell percentage

Seeding of the cells and treatments

U2OS and hTERT RPE-1 cells were transfected with the appropriate siRNAs against luciferase gene (siControl) and MDC1 (siMDC1) (listed in Table S2). A day after transfection cells were trypsinized (TrypLE express, listed in the resource table) and seeded in 96 well plates where the final analysis took place (U2OS: 3000 cells in each well, hTERT RPE-1: 5000 cells in each well). 24 h following cell seeding, cells were treated with specific concentrations of THZ1 inhibitor (0μM, 0.5μM, 1.0μM) and were incubated for 48 h at 37°C, 5%CO_2.

Staining

100μL of staining solution (Hoechst 33342 1:2000, Propidium Iodine_PI 1:1000 (Thermo Fisher Scientific), warm PBS) were added to the 100μL culture medium in each well and cells were incubated for 15 min at 37°C, 5%CO_2. During incubation, plates were protected from light.

Image acquisition

Image acquisition was carried out by Celigo Imaging Cytometer (Nexcelom Bioscience) according to the manufacturer. A 99% well mask size was used to exclude cells close to the edges of wells that would be difficult to analyze. Correction of the background noise and automatic focus was carried out by the machine.

Analysis

The percentage of dead cells was calculated by the number of PI-positive cells (dead cells) divided by the total number of cells in each well. The average from the experimental replicates of each biological replicate was calculated and statistical analysis was carried out via GraphPad Prism (unpaired student's t-test).

Indirect immunofluorescence (IF)

Seeding of the cells

Cells were seeded on autoclaved 12mm coverslips (631-0713, Menzel-Glaser) in appropriate numbers to be 70–80% confluent by the day of the fixation. Coverslips were gently pressed toward the bottom of the plates prior to the seeding to get an even distribution of the cells. Cells were added to the culture vessels which were gently swirled.

Pre-extraction

An additional step was added before the fixation of the cells. The cell medium was aspirated, and cells were washed twice with cold PBS. Pre-extraction solution (PBS, 0.1% Triton X-100) was added to the coverslips and they were incubated for 5 min on ice. Pre-extraction was performed to extract information for the chromatin bound fraction of our proteins of interest. Particularly during this step, the chromatin-unbound nuclear fraction of our target protein was washed away due to the Triton X-100 detergent used in the pre-extraction solution. Coverslips were washed three times with cold PBS and fixation was carried out with 4% Formaldehyde solution (resource table).

Fixation

The cell medium was aspirated, and cells were washed twice with cold PBS. Cells were fixed with 4% Formaldehyde solution (listed in the resource table) for 15 min in RT. The 4% Formaldehyde solution was then aspirated, and cold PBS was added directly. Coverslips were stored at 4°C in PBS-containing Petri dishes until further processing.

Cell permeabilization

Cold PBS was aspirated from dishes with fixed cells and permeabilization buffer (PBS, 1%Triton X-100) was added. Cells were incubated for 10 min at RT before the blocking step. During this step cell membranes are permeabilized so that the primary antibody (and the secondary antibody) can penetrate the cell and nuclear membranes and bind to its target. In addition, protein epitopes are better exposed/accessible during this process, facilitating their recognition by the primary antibodies. Cells were then washed three times with cold PBS and the blocking step was carried out.

Blocking

Blocking of potential non-specific binding sites of the antibodies to the examined cells was performed through incubation of the fixed cells with PBS + blocking buffer (PBS, 0.1% FBS, 0.05%NaN3). This blocking solution contains fetal bovine serum (FBS) as the protein-rich source that occupies any non-specific 'sticky' protein-binding sites of the fixed cells. Cells were incubated with the above blocking buffer for 15 min at RT. Additionally, to maintain the excess protein during the antibody incubation steps, the primary and secondary antibodies were diluted in the same PBS + blocking buffer.

Incubation with the primary antibodies

Primary antibodies were diluted accordingly in the blocking solution and were added to each coverslip (primary antibodies are listed in the resource table). Cells were incubated either for 1 h at RT or overnight at 4°C. Cells were then washed three times with cold PBS (in each wash coverslips were incubated with cold PBS for 5 min) and proceeded to the incubation with the secondary antibody (resource table).

Incubation with the secondary antibodies

Alexa fluor conjugated IgG secondary antibodies were diluted 1:1000 (listed in the resource table) in PBS + blocking buffer together with Hoechst (1:2000, H3570 Invitrogen) and were added to each coverslip. Cells were incubated for 1 h in RT, in the dark, followed by washing 4 times with cold PBS, one time with the PBS + blocking solution and 1 time with ddH2O (in each wash coverslips were incubated with cold PBS for 5 min). Coverslips were then left to dry in the dark.

Mounting

Coverslips were mounted on glass slides in order to proceed to microscopic observation. Vectashield antifade mounting medium (H-1000) was deposited on the glass slides and coverslips were positioned face down on it. Coverslips were then gently pressed toward the glass slide and the excess of the mounting medium was removed by tissue paper. Glass slides were kept at 4°C for at least 24 h prior to microscopic observation, to allow for sufficient hardening of the mounting medium.

X irradiation (X-Rays)

Sample preparation

Cells were seeded in appropriate numbers to reach 70–80% of confluence on the day of the experiment. In the case that X irradiation was combined with BrUTP incorporation assay, cells were seeded on coverslips where the BrUTP incorporation assay was performed. The culture medium was refreshed on the day of irradiation.

X-Rays/incubation of the cells

Culture dishes were transferred to XYLON.SMART 160E/1.5 device (150kV, 6mA, delivering 11.8mGy per second) where the irradiation took place. Cells were X irradiated with 5Gy (this required approximately 7 min using the above-mentioned X-rays source) and then incubated at 37°C for the indicated time points (7 min, 15 min, and 30 min).

BrUTP incorporation assay

Cells were incubated with BrUTP analog. Following the incubation timepoints after X irradiation (7 min, 15 min, and 30 min), coverslips were washed once with warm PBS and were incubated with the permeabilization buffer (20nM Tris pH 7.4, 5mM $MgCl_2$, 0.5mM EGTA, 25% Glycerol, 0.1% Triton X-100, 1mM PMSF, RNase inhibitor 2 Units) for 2 min at RT. During the step of permeabilization, non-engaged RNAPII complexes are removed so that only the engaged ones are triggered to incorporate the BrUTP analog. Aspiration of the permeabilization buffer was followed by the addition of the transcription buffer (100mM KCl, 50mM Tris pH 7.4, 10mM $MgCl_2$, 0.5mM EGTA, 25% Glycerol, 1mM PMSF, RNase inhibitor 2 Units, 1mM ATP, 200nM CTP, 200nM GTP and 200nM BrUTP) and coverslips were incubated at 37°C, 5% CO_2 for 8 min. Then, the coverslips were washed once with cold PBS and fixed with 4% Formaldehyde solution (listed in the resource table) for 15 min at RT. Coverslips were kept in the refrigerator in PBS until the staining procedure.

UVA laser ablation using Nikon confocal microscope equipped with PerkinElmer spinning disk

Sample preparation/cell seeding

Cells were seeded on Lab-Tek chambered coverglasses (# 155380) two days before the live cell imaging experiment. The bottom of these special culture vessels is thin to facilitate Nikon microscope autofocus function during live cell imaging. Cells were treated with 10μM of Bromodeoxyuridine (BrdU) for 24 h prior to the experiment in order for the chromatin to be pre-sensitized. During pre-sensitization, BrdU is incorporated in the DNA of the cells (within 24 h U2OS cells have completed a cell cycle where they incorporate BrdU analog during S phase) sensitizing it toward UVA laser microirradiation and facilitating DSBs formation by using less energy (or power) per pulse (indicating high efficiency of DSB formation). Right before the cells were transferred to the Nikon workstation for live cell imaging, Dulbecco's modified Eagle's medium (DMEM, listed in the resource table) was replaced by $DMEM^{GFP}$-2 medium (MC-102, Evrogen) for the incubation of the cells during the time of visualization. $DMEM^{GFP}$-2 medium increases the photostability of

EGFP fluorescent signal preventing its photobleaching during prolonged excitation. Live cell imaging combined with UVA laser microirradiation was performed at 37°C and 5% CO_2 chamber using Nikon ECLIPSE Ti microscope equipped with PerkinElmer UltraVIEW VoX spinning disk. The Volocity program was used to control the hardware during the live cell imaging experiment.

UVA laser ablation

Single laser Rapp OptoElectronic microscope system with UVA 355nm ablation laser was used to induce DSBs formation at selected subnuclear areas (usually in a stripe shape across the nucleus) and laser settings were manipulated through SysCon software (0.15 power setting, repetition rate 200Hz, pulse energy >60μJ, pulse length<4ns). Live cell imaging was carried out at 37°C in a 5% CO_2 chamber. Cellular response to DSBs was monitored by 63X water-immersion objective and images were acquired in 10-s intervals for a total period of 10 min by ORCA-Flash4.0 camera (HAMAMATSU).

Analysis of protein recruitment kinetics to DSBs

Analysis of the acquired time-lapse videos was carried out by Fiji (ImageJ) software. GFP/YFP intensities on DSB areas were normalized to the intensity of the same fluorophores in the cell nucleus (non-damaged sites of the nucleus) to avoid biases/false effects caused by the heterogeneity in the expression of the GFP/YFP-tagged proteins in the cells following transfection. An average number of cells >10 was analyzed per biological replicate.

UVA laser ablation_ P.A.L.M. Laser Technologies/BrUTP incorporation assay

Sample preparation/cell seeding

U2OS cells were transfected with required specific siRNAs against Luciferase (siControl) and MDC1 gene (siMDC1) purchased from MWG (listed in the resource table). 24 h following siRNA transfection cells were seeded in appropriate numbers on coverslips, 48 h prior to laser micro-irradiation. In the case that the UVA laser ablation technique was combined with BrUTP incorporation assay, cells were not pre-treated with BrdU 24 h prior to exposure to the micro-laser. Laser power was slightly increased because the pre-sensitization step was omitted. Right before the cells were transferred to the Zeiss Axiovert 200 microscope equipped with Axiocam ICc1 for live cell imaging, Dulbecco's modified Eagle's medium (DMEM, listed in the resource table) was replaced by CO_2 Independent Medium (listed in the resource table) for the incubation of the cells during visualization, once CO_2 chamber was not integrated to the microscope.

UVA laser ablation

Zeiss Axiovert 200 microscope is equipped with a PALM UVA pulse nitrogen laser (30Hz, λ = 337μm; Palm Microlaser, Bernied; Germany). 20X air objective was used to (20×/0.8) monitor the cells. The laser output was set to 56% and the energy of the laser was set to 50 and targeted tractable subnuclear DNA damage mainly in the form of DSBs, was generated (usually as a stripe area across the nucleus). Operation of the UVA laser was assisted by PALMRobo-software supplied by the manufacturer.

BrUTP incorporation assay following UVA laser ablation

Coverslips were processed with the permeabilization, and transcription buffers as described above in detail, at specific time points following UVA laser ablation (0 min, 5 min, 10 min). The combination of these two techniques hasn't been used in the past. In a parallel study by Sijie et al., 2021 the authors came up with the same idea of combining laser micro-irradiation with the incorporation of Uridine analog by using the EU click-IT technique, to evaluate *de novo* transcription at sites of DSBs.[80] However, the combination of laser micro-irradiation with BrUTP incorporation is advantageous compared to the experimental strategy followed by Sijie et al., 2021.[80] One of the main advantages is the possibility to extract information regarding *de novo* RNA transcription on DSB sites at a much shorter time point following DNA damage (information that otherwise could be lost). Moreover, permeabilization buffer used as part of this assay (described above) leads to the incorporation of BrUTP analog exclusively by the chromatin-engaged RNAPII complexes unveiling additional information regarding *de novo* RNA synthesis at damaged sites (information about the sequestration of RNAPII on DSBs at very early time-points following DNA damage). Images were acquired through point scanning confocal microscope LSM800 (Zeiss) using 63X oil immersion objective and ZEN software (Zeiss). Quantification of the signal mean intensity was performed via ZEN blue software (Zeiss) at the sites of DSBs using γH2AX as a mask to mark the damaged area in the nuclei. More than 30 cells were analyzed per biological replicate and the average signal intensity of BrUTP was calculated per replicate each time point.

High-content microscopy and quantitative image-based cytometry (QIBC)

Image acquisition

Quantitative image-based cytometry was carried out as previously described.[31] Stained coverslips were mounted on glass slides (Vectashield was used as the mounting medium) and were transferred to Olympus ScanR microscope equipped with ScanR High-content Screening Station with a Pentacube filter system compatible with DAPI, FITC, Cy3, Cy5 and Cy7 fluorescent dyes. Images were acquired at 150 different sites on each coverslip at 20X magnification. Image acquisition was carried out in an automatic and unbiased way via ScanR acquisition software. The automatic focus was performed using the DAPI channel and individual exposures for each fluorophore were set avoiding image saturation. The initial settings were used for all different conditions.

Image analysis

Acquired images were analyzed by ScanR Image Analysis software as described previously.[31] Nuclear compartments were used as masks for the quantification of our proteins of interest including MDC1, γH2AX, 53BP1, RNA polymerase II, and EU analog incorporation based on Click-iT reaction. Hoechst staining was used as the main object and nuclei were detected by the intensity in the DAPI

channel. The threshold was adjusted for each experiment to match the nuclear detection in the preview of nuclear staining. By activating Ignore Border Objects function of the ScanR analysis tool, nuclei at the perimeter/borders of the acquired images were excluded. To include the whole nuclei to use them as our masks for the quantification of our proteins of interest, we activated Fill Holes Within Objects function, too. In that way, nucleoli were not excluded even though the Hoechst staining was weaker at those sub-nuclear compartments. The mean intensity of the desired channels was quantified for each identified nucleus (used as our main object). Nuclear foci were detected and quantified by using the Spot Detection Module of the Sub-object function of the analysis software, at the desired channel by applying a dynamic background correction. Detail, Strength, and Roundness were adjusted so that they match the preview of γH2AX and 53BP1 stained nuclear foci. The setup of the parameters in the analysis software was carried out including:

1. Number of foci per nucleus
2. Circularity factor of the main object
3. Area of the main object
4. Mean and Max intensities of all channels used during image acquisition

The analysis of the results was exported as a txt file and was further analyzed in TIBCO Spotfire® software. In each experimental setup and biological replicate an average number of cells >5000 were analyzed in an automated, unbiased manner with high consistency and low variability, thereby resulting in small error bars and a high degree of statistical significance in terms of any differences between the experimental conditions.

DRB-release-quantitative real-time PCR assay

This small-scale experimental procedure based on the effects of the DRB reversible inhibitor of RNAPII mediated transcription (listed in the resource table), represents a gold standard assay to evaluate the transcription dynamics of RNAPII.[45] U2OS cells were seeded in 60mm diameter Petri dishes and were transfected with siRNAs targeting the Luciferase gene (siControl) and MDC1 gene (siMDC1). Cells were cultivated for 72 h in cell culture conditions (37°C, 5%CO_2) and on the day of the experiment they were treated with 100μM of DRB inhibitor for 4 h. Such 4-h DRB treatment inhibits RNAPII mediated transcription (DRB has been well-characterized as a main inhibitor of the CDK9 subunit of PTEFb complex) while it has no impact on the formation of pre-initiation complexes (PICs) at gene promoter sites. Subsequently, already existing pre-mRNAs are being matured into mRNAs or degraded in case of premature termination during the incubation period. Cells are then washed twice with warm PBS, the DRB inhibitory effect is thereby terminated, and PICs progress through the transcription cycle in a synchronized manner. Total RNAs are extracted from the cells at specific time points following release from DRB and transcription kinetics are evaluated and compared on a small scale by measuring the synthesis of specific pre-mRNAs *via* quantitative real-time PCR.

Total RNA extraction

Total RNA was extracted at 5-min intervals following DRB release until 45 min. The RNeasy Mini Kit (QIAGEN) was used, and the procedure was followed according to the manufacturer's instructions. After final elution, RNA concentrations were calculated *via* nanodrop, RNA quality was evaluated from the ratios of the absorbance at 260nm/280nm and 260nm/230nm, and samples were stored in −80°C.

Reverse transcription

Total RNA of the cells was reverse transcribed by using random hexamers as primers for the reverse transcriptase. High-Capacity cDNA Reverse Transcription Kit (#4368814, Thermo Fisher Scientific) was used according to the manufacturer's instructions.

Quantitative real-time PCR

cDNAs were amplified using specific primers spanning exon-intron junctions of *ITPR1,* and *OPA1* genes that were used as our endogenous reporters. The utilization of endogenous reporter genes instead of exogenous reporters, provided us with more reliable data once transcription kinetics were analyzed on specific genes in their natural chromatin environment. In the case of the *ITPR1* reporter gene, we used primer pairs hybridizing around exon-intron junctions that were both proximal and distal to the transcription start site (TSS) and thus the detected pre-mRNA products following DRB release provided us with a detailed snapshot of the ongoing transcription kinetics (Figures 2E–2G). In the case of *OPA1* reporter gene, primer pairs were used for the detection of the newly synthesized exon of its pre-mRNA as well as for the detection of the splicing product of the same exon (Figures 5A–5C). In that way, the splicing kinetics of the cells are measured on a small experimental scale.

Quantitative real-time PCR was carried out using Fast SYBR Green Master Mix and 7500 Fast Real-Time PCR System (Applied Biosystems). cDNAs were amplified using 40 cycles.

1. Initial DNA denaturation (melting of all dsDNA) at 94°C, for 5 min
2. DNA denaturation at 94°C, for 15 s (x40 cycles)
3. Primer annealing and extension at 60°C, for 30 s (x40 cycles)

Melting curves of the amplified products were generated and evaluated to confirm the specificity of qPCR primers. Detection values were quantified by the comparative threshold cycle method and Ct of each product was extracted. GAPDH was used as our housekeeping gene. ΔCt was calculated as Ct^{GAPDH}-$Ct^{ITPR1/OPA1}$. Values were normalized to the non-treated samples of each

experimental condition. Red dot lines in Figures 2F, 2G, 5B, and 5C indicate the abundance of the *ITPR1* and *OPA1* pre-mRNAs in the non-treated conditions.

Quantitative real-time PCR

Total RNAs were extracted from U2OS cells treated with siControl and siMDC1 and were reversed transcribed as described above. cDNAs were acquired and qPCR was carried out using specific primers spamming exon-exon junctions of *RPS24* and *MYL6* mRNAs (primers sequences are listed in Table S1). Designed primers hybridized to specific exon sequences of *RPS24/MYL6* (Figures S5D, S4E, S5G, and S5H) that were found to be highly abundant and alternatively used upon MDC1 knockdown based on our RNA sequencing data and analysis of isoform usage (described below) (Figures S5C and S5F). Quantitative real-time PCR was carried out using Fast SYBR™ Green Master Mix and 7500 Fast Real-Time PCR System (Applied Biosystems) following the same setup of the thermocycler as described above. Melting curves of the amplified products were generated and evaluated to confirm the specificity of qPCR primers. GAPDH was used as our housekeeping gene. ΔCt was calculated as Ct^{GAPDH}-$Ct^{RPS24/MYL6}$. Values were normalized to the siControl samples in each biological replicate.

RNA sequencing: Nanopore Sequencing Technologies

Library preparation

Total RNA was extracted from U2OS cells 72 h after transfection with siRNAs against Luciferase (siControl), MDC1 (siMDC1), and PLRG1 (siPLRG1). Cells transfected with siControl were either non-treated (NT) or treated with the splicing inhibitor PLAB (5nM) for 3 h. Both PLRG1-depleted cells and siControl cells treated with PLAB served as our positive controls of splicing defected conditions. Library preparation included 12 samples in total (3 independent biological replicates per condition). Total RNA extraction was carried out as previously described using RNeasy Mini Kit (QIAGEN), according to the manufacturer's instructions. Qubit assay was used for the quantification of the eluted RNAs and the ratios of the absorbance at 260nm/280nm and 260nm/230nm were calculated as a quality measurement. Oxford Nanopore Technologies (ONT) kits SQK-PCS109 and SQK-PBK004 were used for the preparation of the cDNA library, according to the manufacturer. The initial input was 70ng of total RNA per condition and cDNA synthesis (using oligo dT primers) combined with strand-switching (using strand-switching primers) was carried out by Maxima H Minus Reverse Transcriptase (Invitrogen, #EP0751). Full-length cDNAs were then amplified by PCR reaction using LongAmp Taq 2X Master Mix (New England Biolabs, #M0287S) and barcoded rapid attachment primers. cDNAs were amplified using 18 cycles. LongAmp Taq Master Mix is used mainly to amplify long DNA strands (up to 30kb). Twelve different barcodes were used for each one of the individual biological replicates of the 4 conditions analyzed (siControl, siPLRG1, siMDC1 and PLAB-treated cells). At the final step of library preparation, rapid 1D sequencing adapters were attached to the amplified barcoded substrates. Barcoded cDNAs were pooled into a 100 fmol library. The library was loaded on an FLO-MIN106 flow cell on an ONT MinION device according to ONT's protocol.

The sequencing was performed for 48 h. Basecalling was performed with Guppy (v3.5.1, ONT) using *–qscore_filtering* and *–min_q score 7* options. Reads passing the quality threshold were demultiplexed and trimmed for adapters with Porechop (v0.2.4). Following Porechop, trimmed reads < Q7 were removed[81] with NanoFilt (v0.2.6), and NanoPlot (v1.29.0) was used for quality inspections and summary statistics. Summary statistics for the resulting, filtered reads are shown in the table below.

Sample	Condition	Read number	Mean read length	Median read length
BC_01	siControl NT	495,981	390.9	218
BC_02	siControl NT	571,460	367.6	194
BC_03	siControl NT	546,122	388.8	225
BC_04	siMDC1	454,331	479.4	359
BC_05	siMDC1	414,506	500.3	381
BC_06	siMDC1	387,584	479.3	318
BC_07	siPLRG1	456,050	402.7	221
BC_08	siPLRG1	481,088	395.4	220
BC_09	siPLRG1	435,639	394.9	231
BC_10	siControl PLAB	474,432	407.6	234
BC_11	siControl PLAB	516,000	393.9	208
BC_12	siControl PLAB	544,778	374.3	190

Analysis of isoform and splicing changes was performed using the Full-Length Alternative Isoform analysis of RNA (FLAIR)[56] workflow as described below. FLAIR was downloaded from https://github.com/BrooksLabUCSC/flair on 2020-03-25. FLAIR was run with hg38 and the GENCODE v32 comprehensive annotation wherever relevant and with default parameters unless otherwise stated. To create a common set of isoforms for all samples, all reads were passed to the FLAIR 'align', 'correct', and 'collapse' (with

–*no_redundant best_only*) modules. Then, this isoform set was supplied to FLAIR 'quantify' together with reads for the pairwise comparisons. The pairwise read counts were then passed to the FLAIR 'diffExp' and 'diffSplice' modules for differential isoform usage and alternative splicing event analyses. FLAIR 'quantify' was run with all samples to obtain read counts for principal component analysis (PCA) which was done using *DESeq2*[82] (v1.30.1) with variance stabilizing transformation. For the downstream PCA and differential isoform usage analyses, only transcripts from annotated genes were considered. The scripts 'predictProductivity.py' and 'plot_isoform_usage.py' available on the FLAIR GitHub page were used to create the isoform usage plots.

DRB/TT$_{chem}$-seq to measure RNAPII progression following release from DRB

DRB/TT$_{chem}$-seq was carried out as previously described with minor modifications.[47] Briefly, control and siMDC1 treated cells were incubated with 100 μM DRB (5,6-dichlorobenzimidazole 1-β-D-ribofuranoside; Sigma-Aldrich, D1916) for 3.5 h and DRB inhibition released for 10, 20, 30 and 40 min by 3 washes pre-warmed PBS. For each time point, newly synthesized RNA was labeled with 1 mM 4-thiourudine (4sU, Biosynth Carbosynth, NT06186) for 10 min immediately prior to harvest by addition of TRIzol (Thermo Fisher, 15,596,026) directly on top of the cell monolayer. Samples were prepared in duplicates for all time points. Total RNA was harvested using TRIzol including an additional chloroform cleanup and isopropanol precipitated. 50 μg of total RNA were spiked in with 0.5 μg of yeast spike-ins (*Saccharomyces cerevisiae* W303a cells labeled with 5mM 4-thiouracil (4tU, Sigma, 440736) for 5 min, see Gregersen et al., 2022 for detailed procedure). RNA was fragmented for 20 min on ice by base hydrolysis and returned to a neutral pH buffer prior to biotinylation as previously described.[47] For the addition of biotin to 4sU residues we used the MTSEA Biotin-XX linker (Biotium, BT90066). Biotinylated RNA was purified by phenol:chloroform and isopropanol precipitation, heat denatured and used for purification with μMACS Streptavidin microbeads (Miltenyi, 130-074-101). 4sU-RNA was eluted from beads using 2 rounds of 100 mM DTT and cleaned up with the RNeasy MinElute Cleanup Kit (Qiagen, 74204) using 1.5x excess of ethanol for the RNA precipitation compared to the supplied protocol to ensure recovery of small RNA fragments. The concentration of 4sU-RNA was measured by Qubit (RNA high sensitivity assay, ThermoFisher Q32852) and the size range was determined by high sensitivity RNA assay on a TapeStation (high sensitivity RNA ScreenTape, Agilent, 5067-5579). 12 ng of 4sU RNA was used for next-generation sequencing library preparation with the NEBNext Ultra II directional RNA kit (NEB, E7760) using Unique Dual Index UMI Adaptors (NEB, E7416) following the protocol for degraded RNA (RIN 1-2) without additional RNA fragmentation. Libraries were amplified using 11 PCR cycles, concentration measured by Qubit (DNA high sensitivity assay) and size distribution assessed using TapeStation (high sensitivity D5000 ScreenTape, Agilent, 5067-5592). The final library size distribution peaked at 350 nt, corresponding to an insert size of 200 nt. Libraries were sequenced on a NextSeq2000 (Illumina) with P3 v100 flow cell (130 cycles) in paired-end mode.

Reads for each sample were marked with UMIs and aligned against the Homo sapiens GRCh38 and Saccharomyces cerevisiae sacCer3 reference genomes with Ensembl release 106 transcript annotations using STAR v2.7.2b.[83] Resulting genome alignment BAM files were filtered off multi-mapped reads with Samtools v1.14 (-q 10) and deduplicated using UMItools.[84] The yeast spike-in was used to account for differences in library size between samples. The reads uniquely mapping to the yeast genome were quantified and used for normalization between merged replicates samples. bigWig files were generated by converting merged BAM files with the deeptools' bamCoverage function and scaled based on spike-in ratios.[85] Spipe-in normalized merged replicates were plotted as metagene using the deeptools' plotProfile function. For measuring transcription wave progression and elongation rate metagene plots were generated from bam files as has been already described.[86]

QUANTIFICATION AND STATISTICAL ANALYSIS

GraphPad Prism (Version 8.0) was used for the statistical analysis. The p value was calculated by unpaired student t-tests. Details about the number of values/biological replicates, can be found in the corresponding figure legends. In all cases, NS: not significant ($p > 0.05$), *: $p < 0.05$, **: $p < 0.01$, ***: $p < 0.001$, and ****: $p < 0.0001$.